

1 Seismo-acoustic and GNSS observations of a record-breaking Black 2 Sea storm: repurposing geophysical sensors for environmental 3 monitoring 4

5 Laura Petrescu^{1,2,*}, Bogdan Antonescu^{1,2}, Sorin Nistor³, Iustin Floroiu^{4,5}, Dragoş Ene¹, Daniela
6 Ghica¹, Constantin Ionescu¹, Andrei Anghel⁴, Mihai Datcu⁴
7

- 8 1. National Institute for Earth Physics, Magurele, Romania
- 9 2. University of Bucharest, Faculty of Physics, Magurele, Romania
- 10 3. University of Oradea, Faculty of Construction, Cadaster and Architecture, Oradea,
11 Romania
- 12 4. Politehnica University of Bucharest, Faculty of Electronics, Telecommunications and
13 Information Technology, Bucharest, Romania
- 14 5. Politehnica University of Bucharest, Doctoral School of Electronics,
15 Telecommunications & Information Technology, Bucharest, Romania
16

17 * laura.petrescu@infp.ro
18

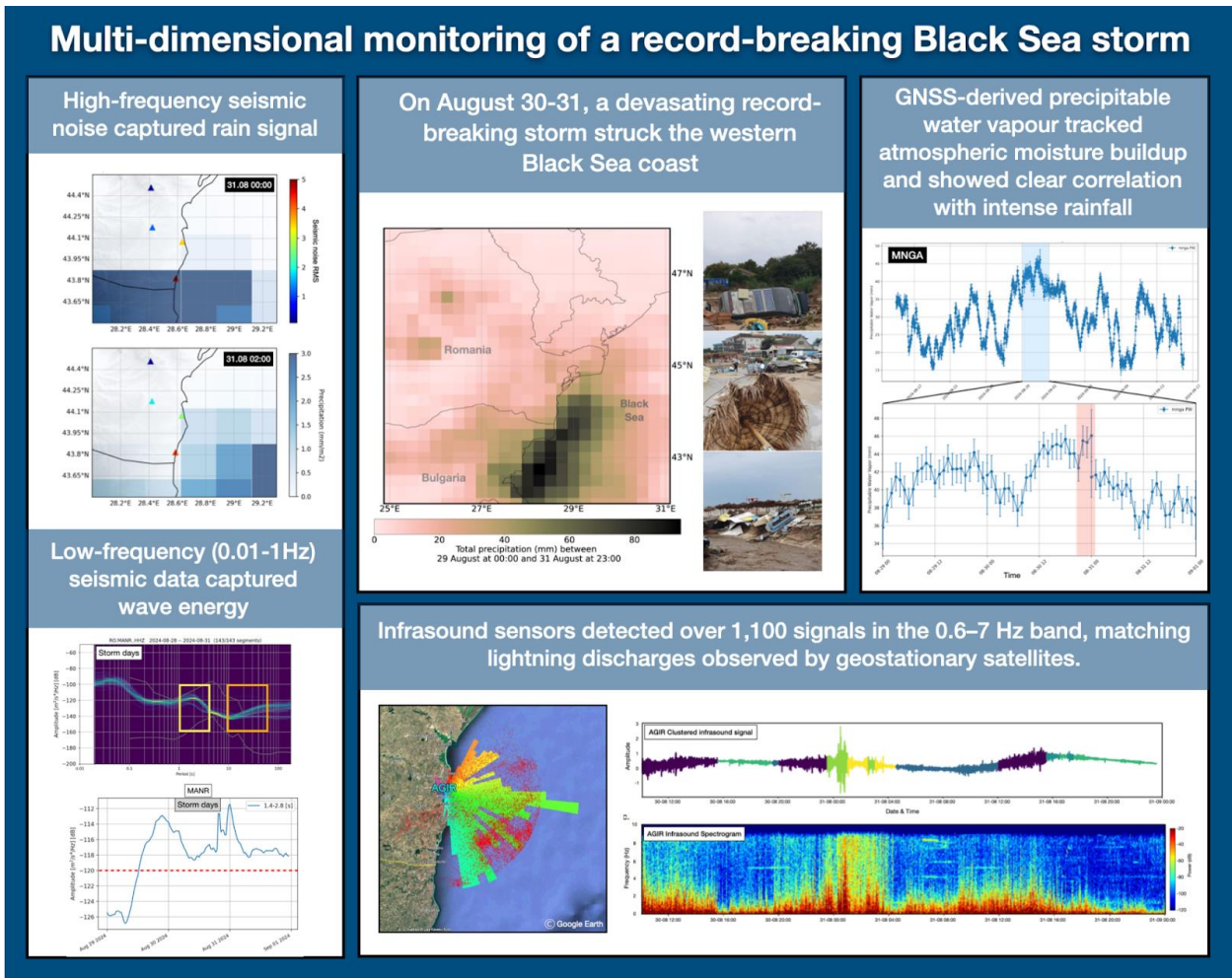
19 Abstract 20

21 In August 2024, a devastating storm struck Romania’s Black Sea coast, setting new precipitation
22 records and highlighting the increasing frequency of extreme weather events. This study explores
23 the integration of non-conventional sensors (seismic, GNSS, infrasound, and satellite data) with
24 ERA5 meteorological reanalysis to monitor storm dynamics. High-frequency (>30 Hz) seismic
25 signals captured precipitation, while microseismic bands (0.1-1Hz) reflected wave-induced ground
26 motion. Analysis of infrasound data via unsupervised learning delineated periods of acoustic
27 quiescence from storm-related activity. The temporal evolution of these infrasound states
28 coincided with distinct patterns in seismic ground motion, suggesting a shared origin in the storm's
29 atmospheric dynamics. The infrasound array also detected over 1,100 signals in the 0.6-7 Hz band,
30 matching lightning discharges observed by geostationary satellites. GNSS data recorded a buildup
31 of precipitable water vapor that peaked concurrently with intense rainfall, following a multi-day
32 increase that preceded the main storm phase. This study highlights the value of integrating diverse,
33 non-traditional datasets to enhance the resolution and depth of storm analysis. Their combined use
34 offers a more holistic understanding of storm evolution and supports [future research on the
35 potential role of multi-sensor observations in improving the development of improved early-
36 warning systems in vulnerable coastal regions.](#)

37

38 **Graphical abstract**

39



40

41

42

43

44

45

46

47

48 **1. Introduction**

49 Climate change has become a critical global issue, with far-reaching effects on weather patterns
50 and the frequency and intensity of extreme events (Stott, 2016). These changes are not only
51 contributing to more severe weather events but also altering the timing, location, and duration of
52 storms, making them harder to predict and manage (Bengtsson et al., 2006). Understanding how
53 to effectively monitor and predict the behavior of storms, particularly extreme ones, is crucial for
54 improving forecasting models, enhancing early warning systems, and mitigating their impacts on
55 both natural and human systems.

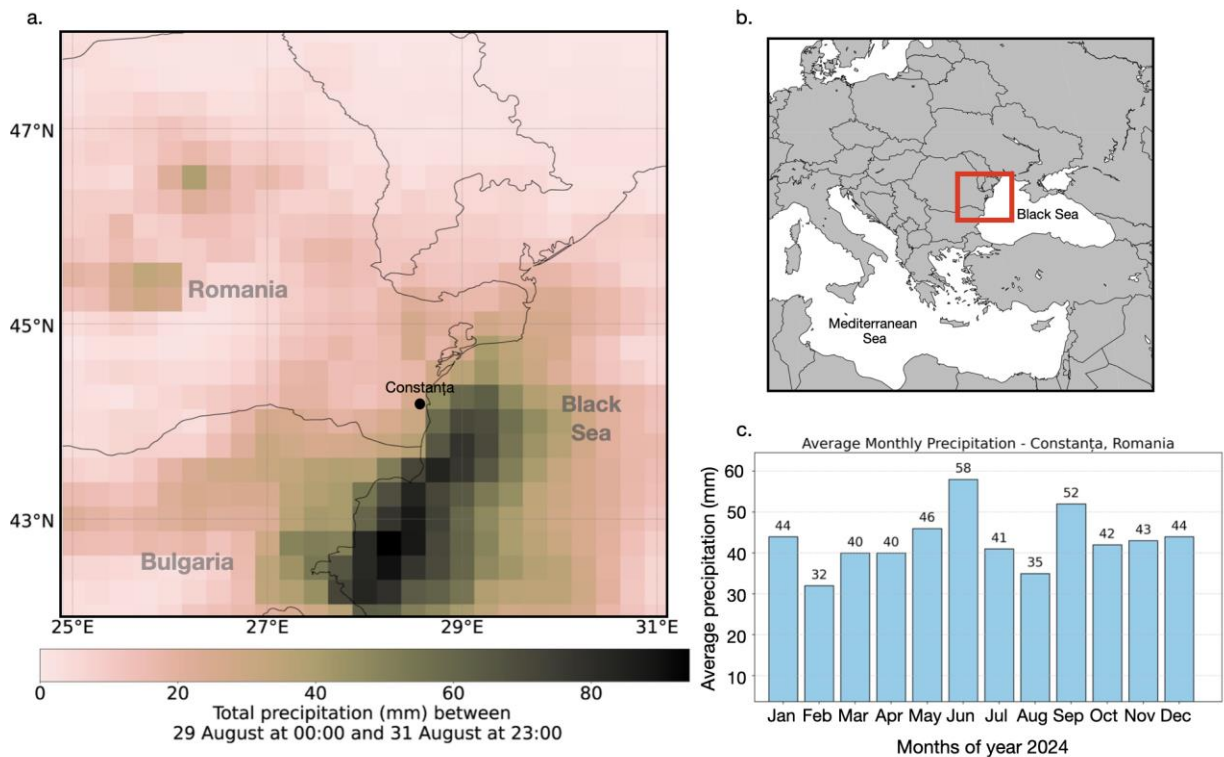
56 Traditional meteorological monitoring relies heavily on ground-based stations, weather radars, and
57 satellite observations to track and predict storm behavior (Kober and Tafferner, 2009). These
58 systems have been the backbone of weather forecasting for decades, providing valuable data on
59 temperature, pressure, wind speed, and precipitation. However, while these methods are effective,
60 they often have limitations in terms of spatial coverage (e.g. Sokol et al., 2021), particularly in
61 remote or hard-to-reach areas. Additionally, they may struggle to capture certain atmospheric
62 phenomena in real-time. As a result, non-conventional monitoring methods are increasingly being
63 integrated into storm tracking efforts to complement existing meteorological approaches (e.g. Bosy
64 et al., 2012; Burtin et al., 2016; Diaz et al., 2023; Coviello et al., 2024).

65 In this context, our study focuses on the integration of alternative environmental datasets, including
66 GNSS stations, infrasound sensors, and seismic data, to track the dynamics of an extreme storm
67 event, as part of a national climate change resilience strategy, implemented through the DTE
68 Climate project (<https://dteclimate.upb.ro/>). GNSS data provide valuable information on
69 atmospheric water vapor, helping to track moisture changes that influence storm formation and
70 intensity (Bosy et al, 2012; Marut et al., 2022). Infrasound sensors detect low-frequency acoustic
71 waves generated by storm activity, such as lightning or large-scale weather system movements
72 like microbaroms (e.g. Landès et al., 2012). Seismic data, though traditionally used for earthquake
73 monitoring, can also record vibrations caused by storm-induced pressure changes, making it useful
74 for detecting rainstorms, floods, or tropical cyclones (e.g. Retailleau and Gualtieri, 2021). Through
75 the integration of these diverse sensor networks, our work highlights their synergy in improving
76 storm detection, monitoring capabilities, and, **potentially**, early warning systems, contributing to
77 more robust climate resilience strategies.

78 **2. Study area and storm overview**

79
80 The Black Sea region (Figure 1) is characterized by a unique combination of geographic and
81 meteorological features that significantly influence its climate and weather patterns. Nestled
82 between Europe and Asia, the Black Sea is bordered by six countries with diverse landscapes, from
83 mountainous areas to flat plains. This geography, combined with the Black Sea's relatively shallow
84 waters compared to oceanic environments and its connection to the Mediterranean through the
85 Bosphorus Strait, creates an environment where rapid changes in weather are common.
86 Understanding the dynamics of these extreme weather events is crucial, as they can have a
87 profound impact on the environment, economy, and daily life in the region. Monitoring such events
88 is key to improving our ability to predict their occurrence and intensity. By studying the complex
89 atmospheric processes that govern these storms, we can enhance predictive models and refine early

90 warning systems, ultimately helping to mitigate the risks and protect the communities and
91 ecosystems most vulnerable to these extreme weather phenomena.



92
93 *Figure 1. a. Total precipitation accumulated (in mm, shaded according to the scale) between 29*
94 *August 00 UTC and 31 August 23:00 UTC extracted from ERA5 data. b. Map of Europe with red*
95 *square marking the study region; c. Average monthly precipitation rates in Constanța, Romania.*

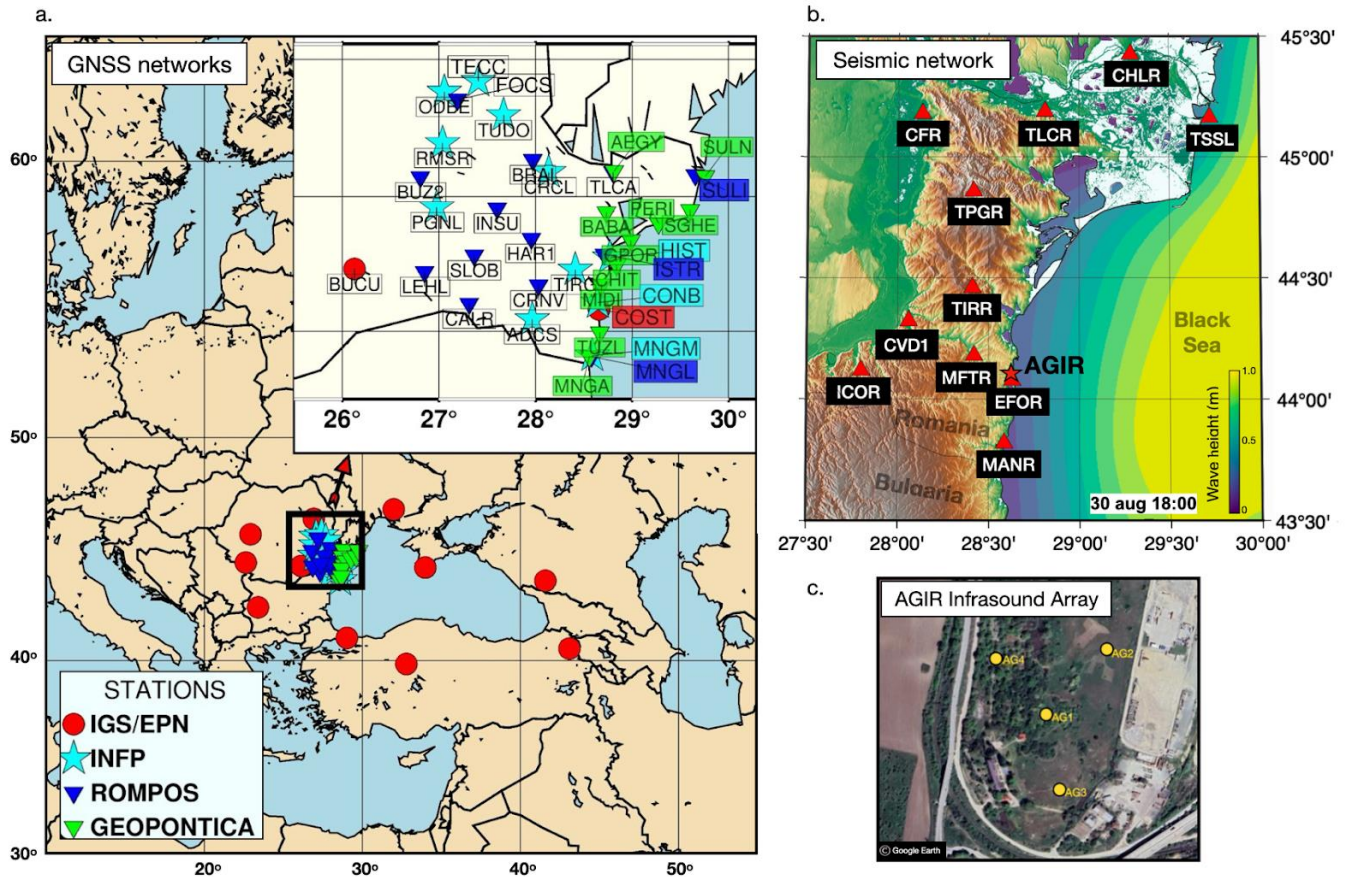
96 In August 2024, Romania experienced severe flooding, largely driven by a storm that brought
97 unusual precipitation patterns to the Black Sea coastal region. Exceptional precipitation totals were
98 recorded over south-eastern Romania in particular in Mangalia (234.7 mm), Agigea (145 mm),
99 and Tuzla (118 mm), leading to significant flooding in coastal towns (Figure 1). Over 800
100 emergency calls prompted large-scale intervention by ISU Dobrogea, focusing on evacuations,
101 debris clearance, and infrastructure restoration (Antonescu et al. 2024). According to the National
102 Meteorological Agency official records ([https://www.meteoromania.ro/clim/caracterizare-](https://www.meteoromania.ro/clim/caracterizare-lunara/cc_2024_08.html)
103 [lunara/cc_2024_08.html](https://www.meteoromania.ro/clim/caracterizare-lunara/cc_2024_08.html)), one of the coastal stations at Mangalia, recorded a total of 343.6 mm of
104 precipitation in August 2024, breaking the previous record of 159.1 mm from 1947, and
105 significantly surpassing the average monthly precipitation values for this area (Figure 1c). A
106 remarkable 234.7 mm of this total fell in a single day on August 31, 2024, highlighting the event's
107 exceptional intensity.

108 An analysis conducted by ClimaMeter (www.climameter.org, Faranda et al. 2024, Antonescu et
109 al. 2024) immediately after the event, showed that low pressure systems similar to the one that
110 caused the floods typically result in reduced rainfall (7 mm day⁻¹, or up to 15% less) in eastern
111 Romania compared to historical trends. However, this particular storm led to a significant local
112 increase in precipitation, particularly in Constanța, one of the coastal cities severely affected by

113 the flooding. In Constanța, daily rainfall reached up to 5 mm day⁻¹, or up to 10% more than usual,
114 marking a notable deviation from the region’s typical weather behavior. The changes in
115 precipitation that contributed to the flooding are largely attributed to human-induced climate
116 change, with natural climate variability likely playing a modest role. As climate change continues
117 to influence weather patterns, understanding the connection between changing precipitation levels
118 and extreme weather events like flooding is crucial for improving forecasting and resilience in the
119 face of such disasters.

120 **3. Data and Methods**

121 The analysis of the storm event integrates a variety of data sources and methodologies to provide
122 a comprehensive understanding of its dynamics. Seismic data, infrasound measurements, GNSS
123 water vapor data, and ERA5 reanalysis data are all utilized to capture different aspects of the
124 storm’s behavior (Figure 2). Seismic data offers insights into ground vibrations and atmospheric
125 disturbances, while infrasound monitoring detects low-frequency acoustic signals generated by
126 lightning and other meteorological phenomena. GNSS water vapor data provides valuable
127 information on atmospheric moisture. Additionally, ERA5 reanalysis data (Hersbach et al. 2020),
128 which provides detailed atmospheric and wave dynamics data, helps contextualize the storm's
129 impact within broader weather patterns. Together, these diverse data sources enable a multifaceted
130 approach to studying the storm and its effects.



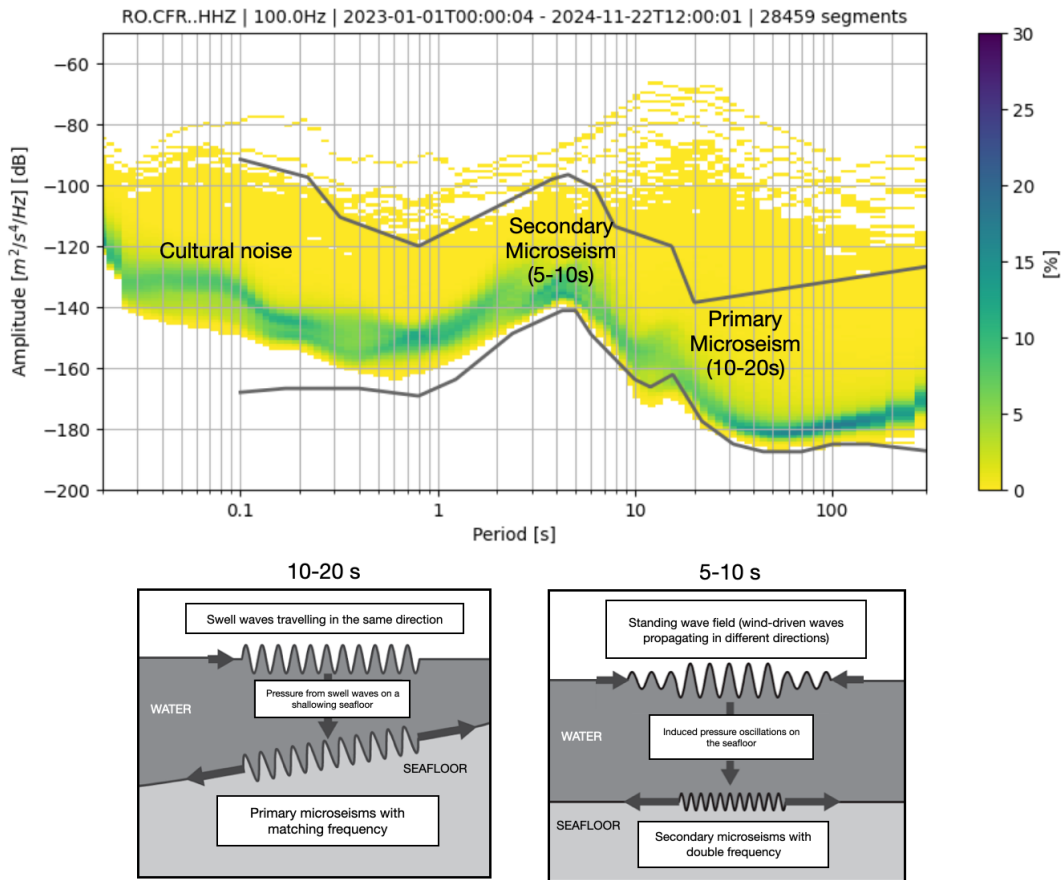
131
 132 *Figure 2. a. Map of Europe and the Black Sea coast showing GNSS stations and their belonging networks*
 133 *used for analysis in this study. b. Map of the Romanian sea coast showing seismic stations (red triangles)*
 134 *and the location of the AGIR infrasound array (star). Coloured contours represent total wave height at*
 135 *18:00 UTC on the 30th of August 2024 from ERA5 reanalysis data. c. The layout of the AGIR infrasound*
 136 *array.*

137
 138 **3.1 Seismic Data**

139 Seismic data represents vibrations of the Earth's surface, commonly referred to as seismic noise.
 140 These low-amplitude movements are recorded across the Earth's surface and are traditionally used
 141 to study the Earth's internal structure and detect earthquakes. Recently, it has increasingly found
 142 applications in meteorology and hydrology, particularly for monitoring weather events (e.g. Dias
 143 et al. 2023; Hua et al., 2023), destructive flood episodes (Burtin et al., 2016), ocean storms, and
 144 tropical cyclones (Gualtieri et al., 2018). Seismic noise can reveal the impact of atmospheric and
 145 oceanic conditions, providing valuable insights into weather events and climate changes (e.g.
 146 Bromirski et al., 2002; Aster et al, 2008; 2023). In particular, seismic data helps track variations
 147 in the Earth's surface caused by factors such as ocean waves, wind, and precipitation, offering a
 148 unique perspective on these phenomena (e.g. Grevemeyer et al., 2000; Borzi et al., 2022).

149 When the seismic noise is analyzed in the frequency domain, two clear peaks emerge in the
 150 spectrum (Figure 3), reflecting distinct types of ocean wave interactions (Koper et al., 2015;

151 Arduin et al., 2019; Tanimoto et al., 2023). The primary peak, observed in the range of 10-20
 152 seconds (0.05-1 Hz), is generated by the impact of "swell" waves traveling in the same direction,
 153 inducing pressure variations in the Earth's crust that match the period of the waves. The secondary
 154 peak, in the range of 5-10 seconds (0.1-0.5 Hz), is produced by wind-driven waves, which
 155 propagate in different directions and generate pressure oscillations on the ocean floor (Ebeling et
 156 al., 2012). These seismic signals directly link ocean conditions with seismic activity (Li et al.,
 157 2020), providing insights into large-scale weather phenomena like ocean storms.



158
 159 *Figure 3. Probabilistic Power Spectral Density (PPSD) of seismic noise for station CFR, over two years,*
 160 *showing key sources of primary and secondary microseisms. Below, sketches illustrate the generation*
 161 *mechanisms: primary microseisms are caused by unidirectional swell waves inducing pressure fluctuations*
 162 *on a shoaling seafloor, while secondary microseisms result from nonlinear interactions of wind-driven*
 163 *waves over deeper water (modified after Ebeling, 2012).*

164 Higher frequencies above 30 Hz are associated with the effects of precipitation and wind, as seen
 165 in studies like Rindraharisaona et al. (2022) or Diaz et al. (2023). These higher-frequency seismic
 166 signals help track more localized weather events, such as storms and heavy rainfall. Seismic data,
 167 when integrated with other meteorological tools, enhances the ability to monitor and predict
 168 weather events.

169 To analyse seismic data, the raw traces are first corrected for instrument response and converted
170 to units of velocity. These are then filtered with bandpass butterworth filters adapted to capture the
171 target signal: low pass filtering (<1 Hz) for wave-seafloor coupled interactions and high pass
172 filtering (>30 Hz) to identify possible signatures of precipitation, essentially induced pressure
173 fluctuations in the ground converted to weak seismic vibrations due to rain drops. Spectrograms
174 of these filtered seismic traces were computed using short-time Fourier transforms implemented
175 in the `scipy.signal` package, with the default 256-sample window length used for each segment,-to
176 visualise signatures of the hydro-meteorological phenomena in the frequency content of ground
177 vibrations.

178 Potential environmental signals in the seismic data were also investigated using power spectral
179 density (PSD) analysis. To account for variations over time, a Probabilistic Power Spectral Density
180 (PPSD) method was applied. The continuous waveform was divided into 1-hour time windows
181 with 50% overlap, and a PSD was computed for each window after instrument-response correction
182 and basic preprocessing. These estimates were combined into a probability distribution, providing
183 a statistical overview of typical and transient noise levels across frequencies. The PPSD was
184 produced using ObsPy (Beyreuther et al., 2010), which handles data gaps and ensures reliable
185 normalization.

186 Temporal variations in PSD amplitudes are also analyzed to track changes in seismic noise at
187 specific frequencies. By extracting PSD values at selected frequencies that are expected to capture
188 primary and secondary microseisms, time series of noise levels are generated. These temporal
189 PSDs allow for the identification of trends and correlations with environmental factors, such as
190 ocean wave activity or weather conditions.

191 **3.2 Acoustic Data**

192 Infrasound waves are low-frequency acoustic waves that are inaudible to the human ear, typically
193 below 20 Hz. These waves are generated by a variety of natural and anthropogenic sources,
194 including meteorological events, volcanic eruptions, earthquakes, and human activities such as
195 explosions and industrial processes (Campus and Christie, 2009; Bondár et al., 2022). In particular,
196 infrasound is often associated with phenomena like thunderstorms, ocean waves, and large-scale
197 atmospheric events, which generate pressure fluctuations that propagate through the atmosphere
198 (e.g. Stopa et al., 2012; Landès et al., 2012; Listowski et al., 2022). These waves provide valuable
199 information about the dynamics of weather systems (e.g. Hupe et al., 2019), making them an
200 essential tool for monitoring and understanding environmental processes (e.g. Brachet et al., 2009;
201 Hupe et al., 2022). Infrasound associated with thunderstorms, primarily generated by acoustic
202 waves from thunder, has been studied previously and shown to be detectable at distances ranging
203 from tens to hundreds of kilometers (e.g., Assink et al., 2008; Sindelarova et al., 2015; Šindelářová
204 et al., 2021). Nevertheless, infrasound arrays detect signals from multiple storm-related sources,
205 not just thunder (e.g., Waxler et al., 2024). In the present study, we build on this understanding by
206 integrating these signals with seismic, satellite, meteorological, and water vapor observations to
207 investigate what these complementary datasets reveal about storm evolution in a coastal
208 environment.

209 For the monitoring of infrasound signals, we use data from an infrasound array system located at
210 Eforie Nord-Agigea, Romania (AGIR, Figure 2). This array consists of multiple sensors, including

211 SIS-1 infrasonic sensors (Seismowave), equipped with global positioning systems (GPS) and noise
212 reduction technology.

213 To analyze the seismo-acoustic characteristics of the August 30-31 Black Sea storm, we used a
214 two-pronged approach: (1) single-station [sensor](#) signal analysis based on feature extraction and
215 unsupervised machine learning, and (2) array-based analysis [using all the sensors of AGIR and](#)
216 classic multi-channel correlation algorithms. Together, these methods provide complementary
217 insights into the acoustic behavior of the storm, capturing both local signal characteristics and
218 spatial coherence across sensors.

219 For the single-station analysis, infrasound data recorded at the AGIR sensor (Figure 2) was
220 segmented into 30-minute windows, and a set of time-frequency features was extracted to
221 characterize the signal dynamics ([Supplementary Material](#)). These features describe how energy
222 and frequency content evolve over time, providing insights into the structure of the infrasound
223 signal. Parameters such as spectral centroid and spectral rolloff are standard descriptors in acoustic
224 signal analysis and are suitable here because they effectively capture shifts in dominant frequency
225 produced by lightning-generated acoustic waves or the passage of pressure disturbances, while
226 spectral flux highlights changes in broadband acoustic energy (Pásztor et al., 2023). Spectral
227 entropy reflects the complexity of the frequency distribution, which increases during turbulent
228 atmospheric conditions, and the zero-crossing rate, mean, and variance of the power spectrum
229 summarize overall activity and variability. This feature set provides a compact representation of
230 the signal suitable for unsupervised machine-learning approaches such as clustering, techniques
231 widely used in data mining to identify patterns in multidimensional time-frequency data (e.g.,
232 Coates and Ng, 2012), and allows us to distinguish physically interpretable stages of storm-induced
233 changes in the infrasound wavefield.

234 The extracted features were used as input for K-Means clustering (MacQueen, 1967), an
235 unsupervised machine learning algorithm that partitions data into a predefined number of groups;
236 ~~in this case, six seven~~. K-Means minimizes within-cluster variance by iteratively assigning feature
237 vectors to the nearest cluster centroid and updating the centroids based on the grouped data. This
238 clustering method enables the identification of distinct acoustic patterns in the signal (e.g. Pásztor
239 et al., 2023), offering a data-driven way to segment the storm’s infrasound profile without
240 requiring prior labels or assumptions. [Prior to clustering, the features were standardized using z-](#)
241 [score normalization, to ensure comparable scaling across variables](#). The optimal number of
242 clusters was determined using the elbow method, which evaluates within-cluster variance as a
243 function of cluster number ([Supplementary Material](#)). To select the most informative features, we
244 applied covariance pruning, and the temporal evolution of the features was visualized to ensure
245 meaningful representation. This procedure resulted in six clusters, providing a balanced
246 representation of the infrasound dynamics while avoiding over-segmentation or overfitting. By
247 combining multiple features in the clustering, this method captures the evolving acoustic states of
248 the storm in a compact, interpretable form.

249 In parallel with the single-station analysis, we also applied the Progressive Multi-Channel
250 Correlation (PMCC) method, as implemented in the DTK-PMCC software (Cansi and Le Pichon,
251 2008; Le Pichon et al., 2010) to detect and analyze coherent acoustic signals across an infrasound
252 array. The PMCC method targets signals generated by atmospheric sources such as lightning (i.e.,
253 associated thunders) or other pressure disturbances, operating in the low-frequency range of 0.7 to

254 7 Hz. It is specifically suited for mini-array configurations, where signal coherence between
255 closely spaced sensors can be exploited for precise signal detection and characterization.

256 The PMCC algorithm was implemented using a multi-resolution configuration following the
257 standardization proposed by Garcés (2013), with window lengths and frequency bands arranged
258 in third-octave bands. A total of 19 frequency bands were used, covering 0.1-7 Hz. Window
259 lengths decrease logarithmically with frequency, ranging from 258 s in the lowest band to 4 s in
260 the highest band. A 10% time step was applied (corresponding to 90% overlap between
261 consecutive windows), and this scheme repeats every decade. Within each time-frequency
262 segment, cross-correlations are computed between all sensor pairs to identify coherent wavefronts,
263 signals that exhibit consistent arrival times across the array. From these detections, PMCC
264 estimates several key propagation parameters, including backazimuth (the direction of arrival),
265 horizontal trace velocity, amplitude, duration, and dominant frequency. This approach is
266 particularly effective in noisy environments and enables the discrimination of storm-generated
267 infrasound from background signals or unrelated acoustic sources. The algorithm's output consists
268 of a time-frequency map of signal detections enriched with physical metadata, allowing for
269 detailed interpretation of the storm's acoustic footprint and its temporal evolution.

270 3.3 Satellite Observations

271 We also incorporated data from the Meteosat Third Generation (MTG) satellite system (Holmlund
272 et al., 2021), specifically from its Lightning Imager (LI) sensor (Viticchie et al., 2020). The MTG
273 satellites operate in geostationary orbit at approximately 36,000 km altitude, providing continuous
274 observations over Europe, Africa, and surrounding waters. The Lightning Imager detects cloud-
275 to-cloud, cloud-to-ground, and intra-cloud lightning flashes using four cameras that collectively
276 cover 86% of the Earth's visible disc from the satellite's perspective.

277 For this study, we used Level 2 group data, which includes the geographical coordinates and timing
278 of each detected flash. [The MTG Lightning Imager detects total lightning \(cloud-to-cloud and
279 cloud-to-ground\) optically at 777 nm, with 4.5 km pixel resolution at the sub-satellite point and
280 1 ms frame rate \(Holmlund et al., 2021; Kokou, 2023\). Level-2 achieves detection efficiencies of
281 ~80-90%, capturing even weak flashes reliably, with false alarm rates <0.3 \(Enno et al., 2025\).
282 Flash geolocation uncertainty reaches 5-10 km near the edge of the instrument's field of view,
283 where off-nadir viewing geometry amplifies parallax effects \(Bližňák & Sokol, 2026\).](#) By mapping
284 these detections, we were able to analyze the spatial distribution and temporal evolution of the
285 storm's lightning activity. The dataset also offered insights into the storm's intensity and structure,
286 complementing other meteorological observations.

287 Associations between infrasound detections and lightning flashes detected by MTG within 50 km
288 of the AGIR infrasound station were investigated by assuming direct-path acoustic propagation
289 and a correspondence between infrasound time-of-arrival and the MTG lightning discharge time
290 (after Assink et al., 2008):

$$291 t = t_{\text{MTG}} + d/c + \Delta t,$$

292 where d is the distance between the lightning discharge and the infrasound station, $c = 340\text{m/s}$,
293 and $\Delta t = \pm 10\text{s}$ accounts for timing uncertainty [associated with the simplified propagation](#)

294 assumption. In particular, infrasound travel time from thunder sources can vary due to atmospheric
295 temperature and wind variations along the propagation path, which affect the effective sound speed
296 and may introduce deviations from the assumed constant-velocity, straight-path propagation.
297 Additionally, a maximum angular deviation of 10° between the observed infrasound backazimuth
298 and the MTG-derived backazimuth is permitted for an association to be accepted.

299 **3.4 GNSS Data**

300 The use of GNSS technology for atmospheric monitoring provides a powerful tool for analyzing
301 extreme weather events. Beyond its well-known applications in navigation and timing, GNSS has
302 become a reliable method for sensing tropospheric water vapour, an essential driver of weather
303 systems and a key variable in forecasting models (Guerova et al., 2016; Vaquero-Martínez and
304 Antón, 2021). Over the past two decades, ground-based GNSS networks in Europe have
305 contributed significantly to operational meteorology by providing near real-time estimates of
306 atmospheric water vapour, aiding in the detection and tracking of severe weather, including heavy
307 rainfall and storms (Karabatić et al., 2011; Priego et al., 2017; Jones et al., 2020). These high-
308 resolution observations have proven valuable for both nowcasting and validating numerical
309 weather prediction models (Wilgan et al., 2015; Bosy et al., 2012; Awange, 2012).

310 In this study, GNSS data were collected from several networks (Figure 2), including the
311 International GNSS Service (IGS, Johnston et al., 2017), the EUREF Permanent Network (EPN,
312 Bruyninx et al., 2012), the Romanian Position Determination System (ROMPOS, Iliescu et al.,
313 2019), and GEOPONTICA (Dimitriu et al., 2017). A total of 37 permanent GNSS stations were
314 analyzed over a 30-day period, with the rainiest interval selected at the midpoint of the study
315 period. These stations provide high-quality, continuous observations critical for atmospheric
316 monitoring.

317 The data were processed using a double-differenced, ionosphere-free combination of L1 and L2
318 carrier phases. This approach helps minimize errors such as ionospheric delays, satellite clock
319 biases, and other common atmospheric effects. The resulting Zenith Tropospheric Delay (ZTD)
320 values were then corrected using the Vienna Mapping Functions 3 (VMF3, Landskron et al., 2018),
321 which improves the accuracy of ZTD by accounting for variations in the troposphere's atmospheric
322 conditions. Once the ZTD was refined, it was converted into integrated precipitable water vapor
323 (PWV) using surface meteorological data (temperature and pressure) from co-located weather
324 stations, following the method outlined by Bosy et al. (2012). This process allowed for the
325 derivation of high-resolution atmospheric water vapor content, critical for analyzing the dynamics
326 of the extreme storm event over the Black Sea. By combining GNSS-derived PWV with data from
327 other observational sources, the study captured the temporal and spatial variations in atmospheric
328 moisture, offering valuable insights into the storm's development and intensity.

329 **3.5 Meteorological Data**

330 To compare the infrasound signals captured during the Black Sea extreme storm event, we
331 extracted meteorological data from the open-access ERA5 reanalysis dataset, produced by the
332 European Centre for Medium-Range Weather Forecasts (ECMWF). This dataset provides a
333 comprehensive record of global weather conditions from 1950 to the present (Hersbach et al.,
334 2023). ERA5 combines observational data and advanced numerical models to generate [relatively](#)

335 high-resolution atmospheric parameters compared with earlier global reanalyses, including
336 precipitation (Figure 1), wind speed, and wave height. ERA5 has been extensively validated (Jiao
337 et al., 2021; Wu et al., 2022; Soci et al., 2024) and is widely used in studies of storm evolution and
338 precipitation dynamics (e.g. Dullart et al., 2020; Tiberia et al., 2021; Price et al., 2025), making it
339 a suitable choice for the mesoscale processes examined here.

340 For our study, the ERA5 data was used to track the meteorological context of the storm, offering
341 insights into the intensity of precipitation, the evolution of wind patterns, and the development of
342 oceanic wave heights. With a high temporal resolution of 1 hour and spatial resolution of $0.25^\circ \times$
343 0.25° resolution, ERA5 allows for a detailed mesoscale comparison of the storm's meteorological
344 characteristics over time. While its spatial averaging cannot resolve localized convective-scale
345 precipitation, it provides a vital benchmark for qualitative comparisons and for testing multi-sensor
346 monitoring potential. These comparisons help us understand the storm's dynamics and assess its
347 impact, further enhancing the interpretation of infrasound signals and aiding in future storm
348 prediction and monitoring efforts. The open-access nature of ERA5 ensures broad accessibility,
349 contributing to the transparency and reproducibility of our storm analysis (Copernicus Climate
350 Change Service, Climate Data Store, 2023).

351 4. Results

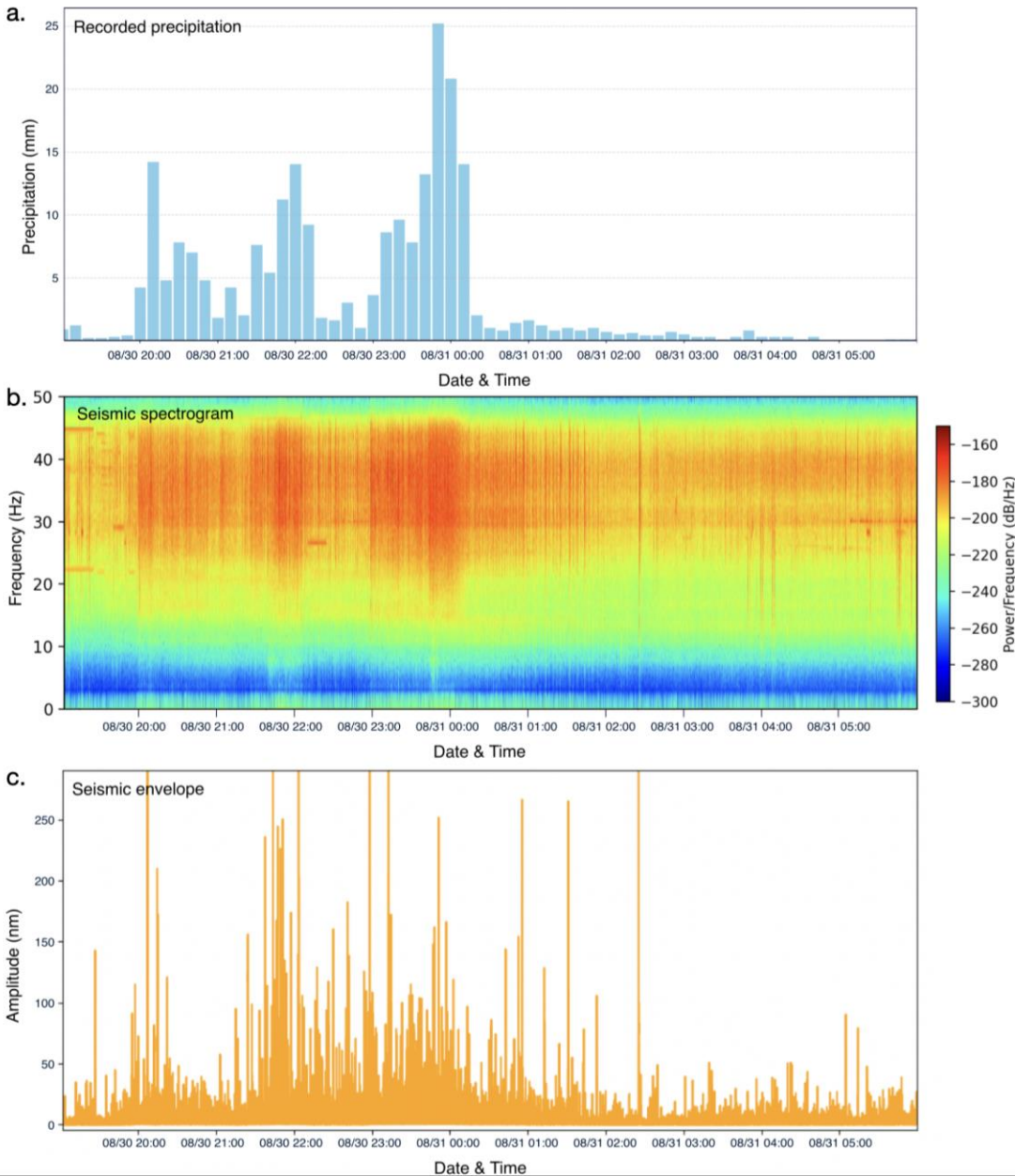
352 4.1 Seismic signatures of storm evolution

353 High frequency (>30 Hz) analysis of seismic noise reveals strong signals during periods of intense
354 rainfall (Figure 4). Specifically, the displacement envelope at station MANR and its spectrogram
355 for 30 August, 12:00 UTC to 31 August, 06:00 UTC (Figures 4b, c) reveal strong signal around
356 midnight, when recorded precipitation exceeded 20 mm per 10 minutes. Similar temporal patterns
357 in the seismic spectrogram were also visible when compared with hourly precipitation levels from
358 ERA5, indicating that the high amplitude of energy observed above 30 Hz is most plausibly
359 generated by raindrop impacts.

360 However, this correspondence is not uniform across all rainfall episodes. While the main
361 precipitation maximum on 30-31 August produces a clear and sustained seismic response, several
362 lower-intensity precipitation pulses show a much weaker or no recognizable signature in either the
363 seismic envelope or spectrogram. This behaviour is consistent with previous work (e.g.,
364 Rindraharisaona et al., 2022), which demonstrates that only rainfall above a certain intensity, or
365 involving sufficiently large drops, generates impact forces strong enough to be detected by
366 broadband seismometers. Our observations therefore reflect both strong positive correlations
367 during intense rainfall and the lack of seismic expression for weaker precipitation. This selective
368 sensitivity supports the interpretation that high-frequency seismic noise can reliably track reflect
369 strong rainfall peaks but is less responsive to light or moderate precipitation, an important nuance
370 when interpreting multi-sensor relationships in this study.

371 Anthropogenic seismic noise is typically strongest at low to mid frequencies (<25 Hz), where day-
372 night variations reflect traffic, human activity, and transient signals from machinery, while higher-
373 frequency bands (25-45 Hz) may include periodic contributions from rotating equipment (e.g.,
374 Gross & Ritter, 2008; Diaz et al., 2017). The bandwidth targeting rainfall in this case is between

375 30-50 Hz, which is above the dominant frequency content of most anthropogenic sources and
376 overlaps with raindrop-impact energy documented in recent rainfall-seismic studies.

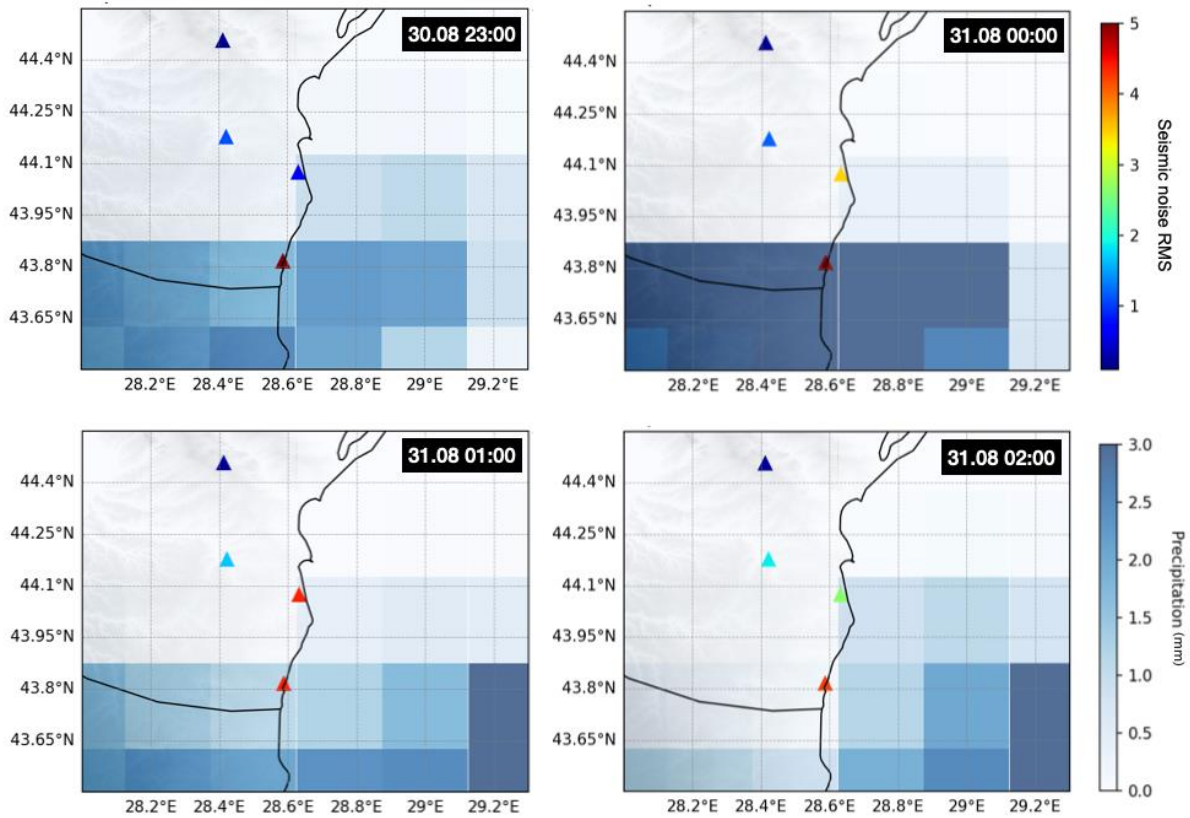


377

378 *Figure 4. High frequency (30-50Hz) observations of the storm at station MANR. a. Time series of total*
379 *precipitation every 10 minutes from the ANM station at Mangalia b. Spectrogram of the seismic time series*
380 *for station MANR. c. Envelope of the displacement seismogram at station MANR.*

381 To visualise the signature of the storm passing over the network of broadband seismic stations in
382 the coastal area, we also plotted the hourly precipitation values with the hourly root-mean-square
383 amplitudes of the high-frequency (>30 Hz) seismic velocity envelopes recorded at seismic stations.
384 Figure 5 shows four snapshots of hourly plots of gridded precipitation data from ERA5, which
385 have a lower amplitude than point measurements at the Mangalia station, due to the averaging over

386 the grid block. This figure presents a temporal coincidence between changing precipitation patterns
 387 from ERA5 data and the amplitudes of high-frequency seismic noise. This observation further
 388 supports the likelihood of a causal relationship. These high-frequency seismic signals could
 389 potentially be ~~monitored in~~ explored as a near real time indicator of ~~to flag~~ intense rainfall events,
 390 providing a conceptual basis for a simple streaming detection approach.



391

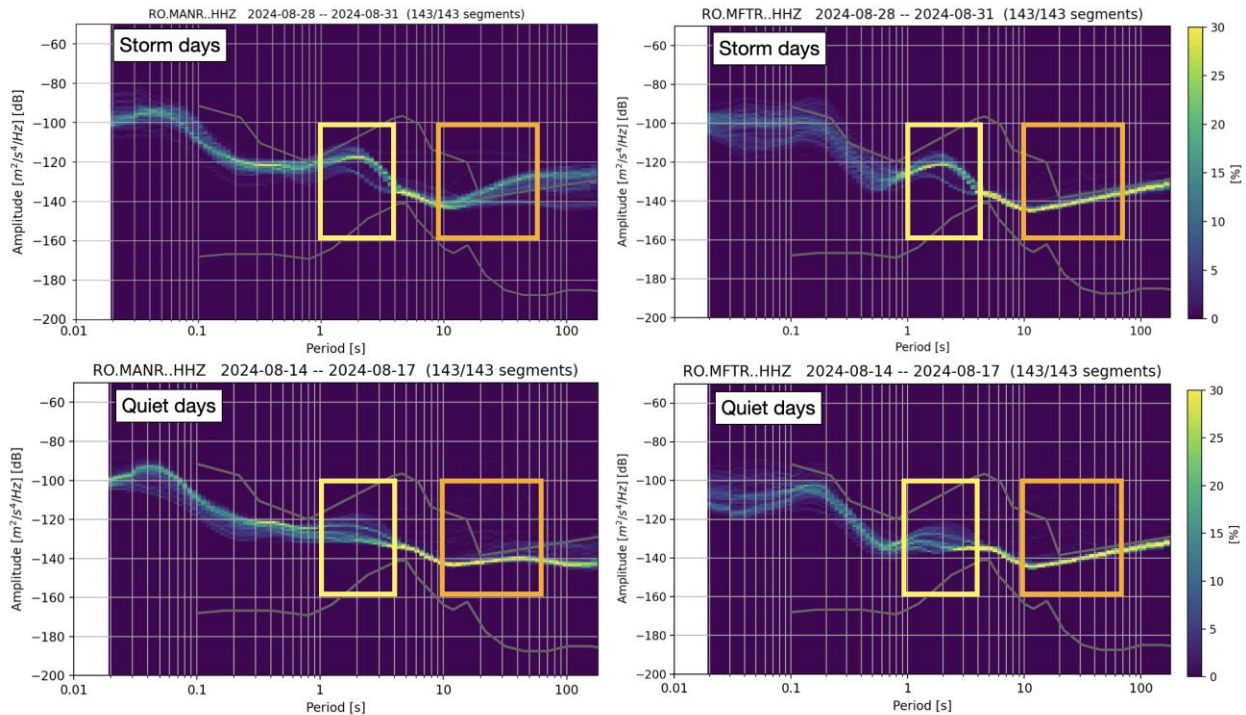
392 *Figure 5. Distribution of hourly RMS of high pass filtered (>30 Hz) seismograms and precipitation data.*
 393 *Colours indicate hourly RMS amplitude of velocity envelopes filtered 30-50 Hz. Background coloured*
 394 *grid indicates the total precipitation (mm) from ERA5 data.*

395 The analysis of the microseismic noise frequency band is closely linked to the interaction between
 396 ocean waves and the seafloor, which is influenced by storm conditions. To assess the storm's
 397 impact, we analyze the PPSD (Probabilistic Power Spectral Density) of noise recorded at several
 398 stations during both storm and quiet days, using the latter as a baseline. Figure 6 shows examples
 399 of PPSD at stations MANR and MFTR (Figure 2), revealing differences in PSD amplitudes across
 400 the primary and secondary microseismic bands. These differences indicate the presence of high-
 401 intensity wind-driven waves and swell energy in the sea.

402 The secondary microseismic band, in particular, shows a significant rise in amplitude during
 403 storms, ~~driven by wind induced pressure fluctuations in the shoaling seafloor~~ (Figure 3, Ebeling
 404 ~~et al., 2012).~~ consistent with established mechanisms linking storm-driven wave activity and
 405 seafloor pressure fluctuations (Figure 3) to enhanced secondary microseism generation, while local

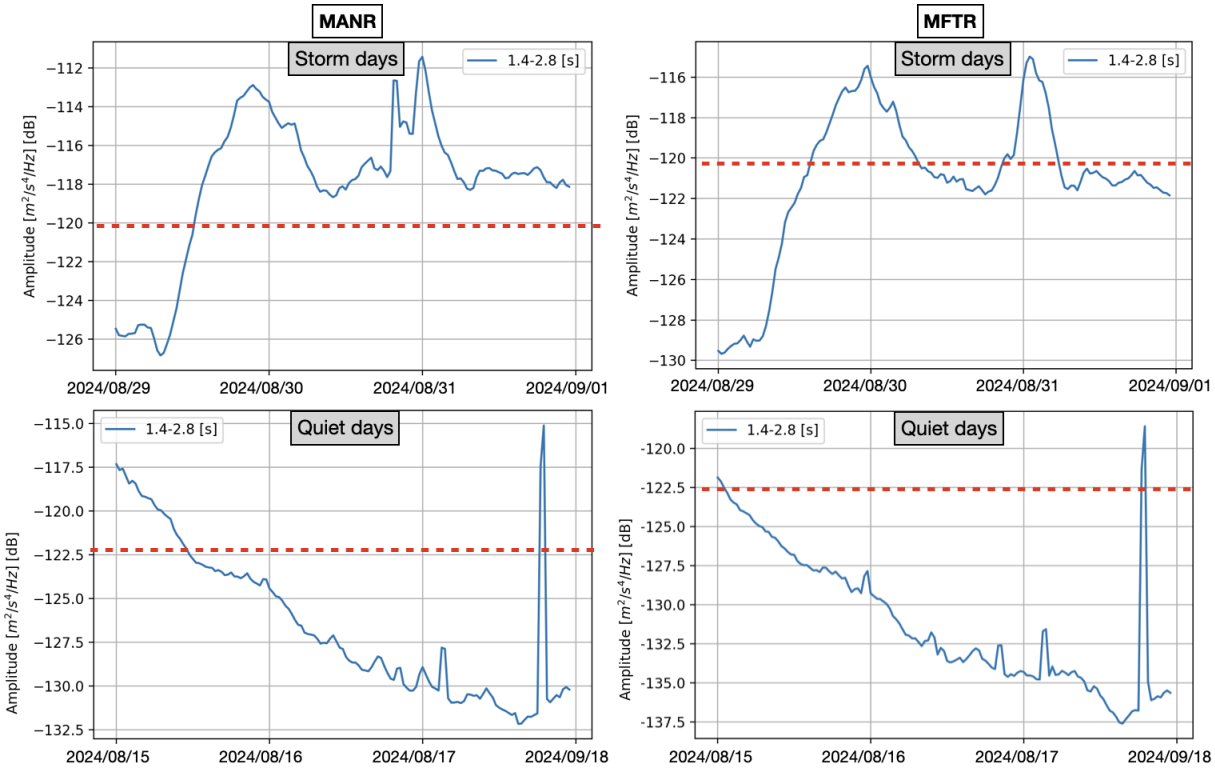
406 factors such as bathymetry or wave direction may modulate the response (Bromirski et al., 2002;
 407 Ebeling et al., 2012; Arduin et al., 2019). On quiet days, the PSD remains consistently lower,
 408 typically staying below the -120 dB threshold. This stark contrast emphasizes the role of
 409 atmospheric conditions in modulating seismic noise, with storms causing a notable increase in
 410 energy across both frequency bands. The temporal evolution of the PSD values (Figure 7) further
 411 highlights the storm's impact, with fluctuations corresponding to changes in environmental factors,
 412 reinforcing the connection between storm activity and the observed seismic signals.

413



414
 415 *Figure 6. Probabilistic Power Spectral Density (PPSD) plots for two seismic stations near the Black Sea*
 416 *coast capturing the target storm signal in the microseismic bandwidths (marked with rectangles). The top*
 417 *panels show the PPSD distributions across frequencies, indicating the probability of power spectral*
 418 *density values in percentage for days including the Black Sea storm. The bottom panels show PPSD for*
 419 *days with no recorded events.*

420 Anthropogenic seismic noise does not significantly affect the microseismic band (0.1-1 Hz).
 421 Human-generated vibrations predominantly occupy frequencies above 1 Hz, while long-period
 422 microseisms are produced by ocean wave interactions and are coherent over large distances. The
 423 temporal evolution of the microseismic energy observed in this study matches changes in wave
 424 state associated with the storm rather than any local activity. Similar to the findings of Gross &
 425 Ritter (2009), the sub-Hz frequency range is dominated by natural sources, with anthropogenic
 426 contributions being negligible.



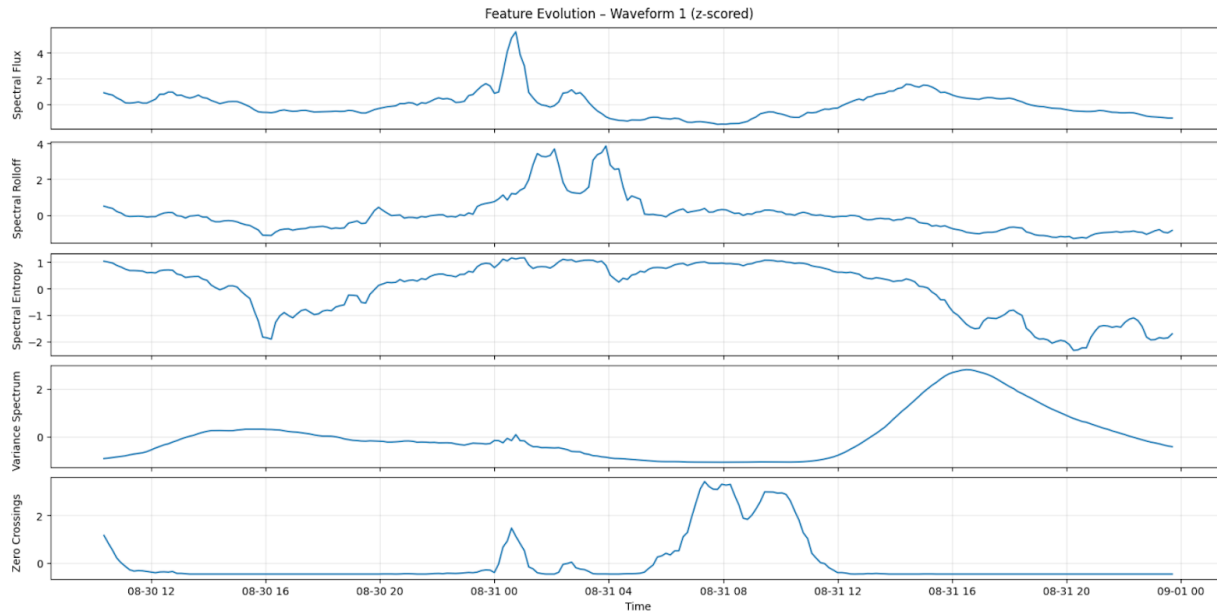
427

428 *Figure 7. Temporal PSDs for two seismic stations near the Black Sea Coast in the secondary microseismic*
 429 *band showing significantly higher values (>-120 dB) during stormy days compared to days without*
 430 *recorded precipitation.*

431 4.2 Infrasound and satellite lightning observations

432 4.2.1 Single-station feature extraction

433 The evolution of time-frequency features over the duration of the Black Sea storm revealed distinct
 434 patterns in the infrasound signal (Figures 8 and 9). Centroid and rolloff show parallel behavior
 435 because they are both frequency-domain descriptors tied to the distribution of spectral energy, and
 436 so both respond strongly to the same uplift in energy during the storm's peak. Spectral flux, by
 437 contrast, quantifies inter-frame spectral change, so its peak occurs where the spectrum transitions
 438 most rapidly, even when that does not coincide with the maximum absolute energy (e.g. Pásztor
 439 et al., 2023). Finally, the zero-crossing rate reflects time-domain volatility, not spectral shape,
 440 which explains its distinct pattern, such as the storm's later stages may introduce broadband
 441 turbulence or noise components that boost zero crossings independently of the spectral shifts
 442 visible in the first two panels. While the individual features varied over time, it is the combination
 443 of these features through K-means clustering that effectively identifies the time frame
 444 corresponding to the main precipitation episode. Zero-crossings exhibited more variable patterns,
 445 reflecting high-frequency fluctuations, but the joint clustering of all features robustly captures the
 446 timing of the storm's most intense phases.

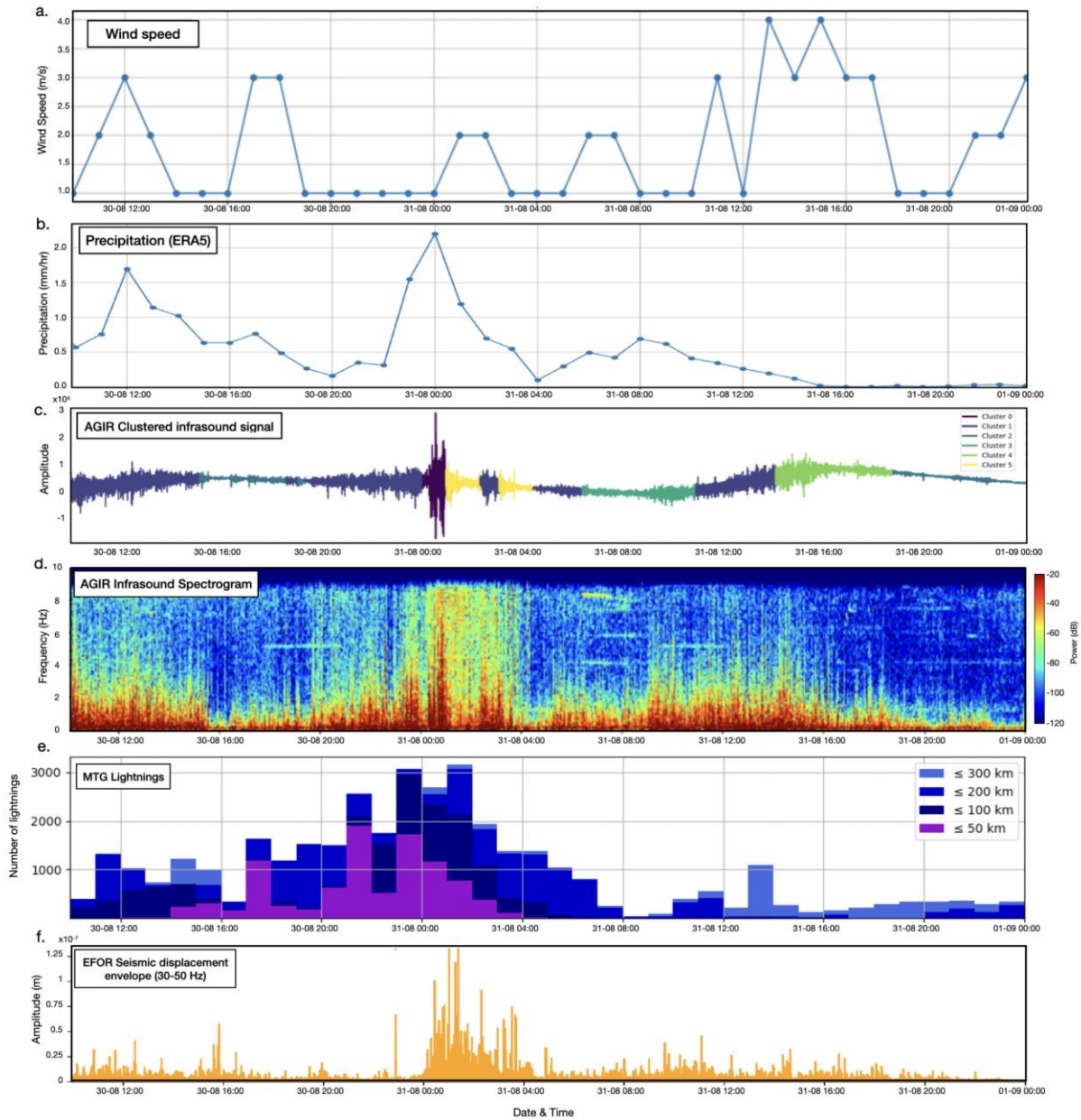


447

448 *Figure 8. Time-frequency feature analysis for the single-station infrasound signal recorded at AGIR during*
 449 *the Black Sea Storm.*

450 K-means clustering separated the acoustic data into six groups with distinct spectral and amplitude
 451 characteristics (Figure 9). These clusters highlight acoustic states that may relate to different
 452 environmental conditions during the monitoring period. For example, Cluster 0 coincides with
 453 periods of intense precipitation and stronger winds, and also aligns with enhanced lightning
 454 activity, suggesting a link with the most energetic phases of the convective system. while Cluster
 455 1 captures intervals with moderate amplitudes but persistently elevated background acoustic
 456 levels, without corresponding rainfall or wind peaks, and with comparatively reduced lightning
 457 occurrence. Cluster 2 reflects calmer conditions with low amplitudes and little or no precipitation
 458 and minimal lightning activity. Transitional patterns also arise, such as Cluster 3, which appear
 459 before intervals grouped in Cluster 1 and mark intermediate acoustic activity. Overall, the
 460 clustering approach demonstrates that combining multiple features reveals consistent acoustic
 461 regimes and can help differentiate environmental conditions, without relying on any single
 462 parameter.

463 Interestingly, the spectral content of the infrasound signal showed similarities to seismic signal
 464 envelopes, particularly in the high frequency ranges (Figure 9), which may suggest a connection
 465 between the atmospheric pressure waves detected by infrasound and the ground vibrations
 466 captured by seismic instruments. When considered alongside the temporal evolution of lightning
 467 activity, this overlap implies that both seismic and infrasound signals could be complementary in
 468 capturing different aspects of storm dynamics, with seismic signals reflecting ground vibrations
 469 and infrasound capturing the atmospheric processes, and lightning indicating convective intensity.



470
 471 *Figure 9. Clustering results of infrasound signals recorded at AGIR from the August Black Sea storm event*
 472 *compared with precipitation data and seismic signal from EFOR station. a. Wind speed per hour measured*
 473 *at ANM meteorological station Constanta; b. Average precipitation data from $1^{\circ} \times 1^{\circ}$ around AGIR. c. Raw*
 474 *infrasound signal recorded at the AGIR sensor during the period of August 30-31, 2024, with different*
 475 *segments color-coded according to the cluster they belong to, based on K-means clustering of 30-minute*
 476 *time-frequency feature windows. d. The corresponding spectrogram generated using Blackman windowing*
 477 *with 128 samples and 70% overlap; e. Number of lightnings detected by the MTG satellite. f. Seismic*
 478 *displacement envelope at station EFOR, filtered between 30-50 Hz.*

479

480

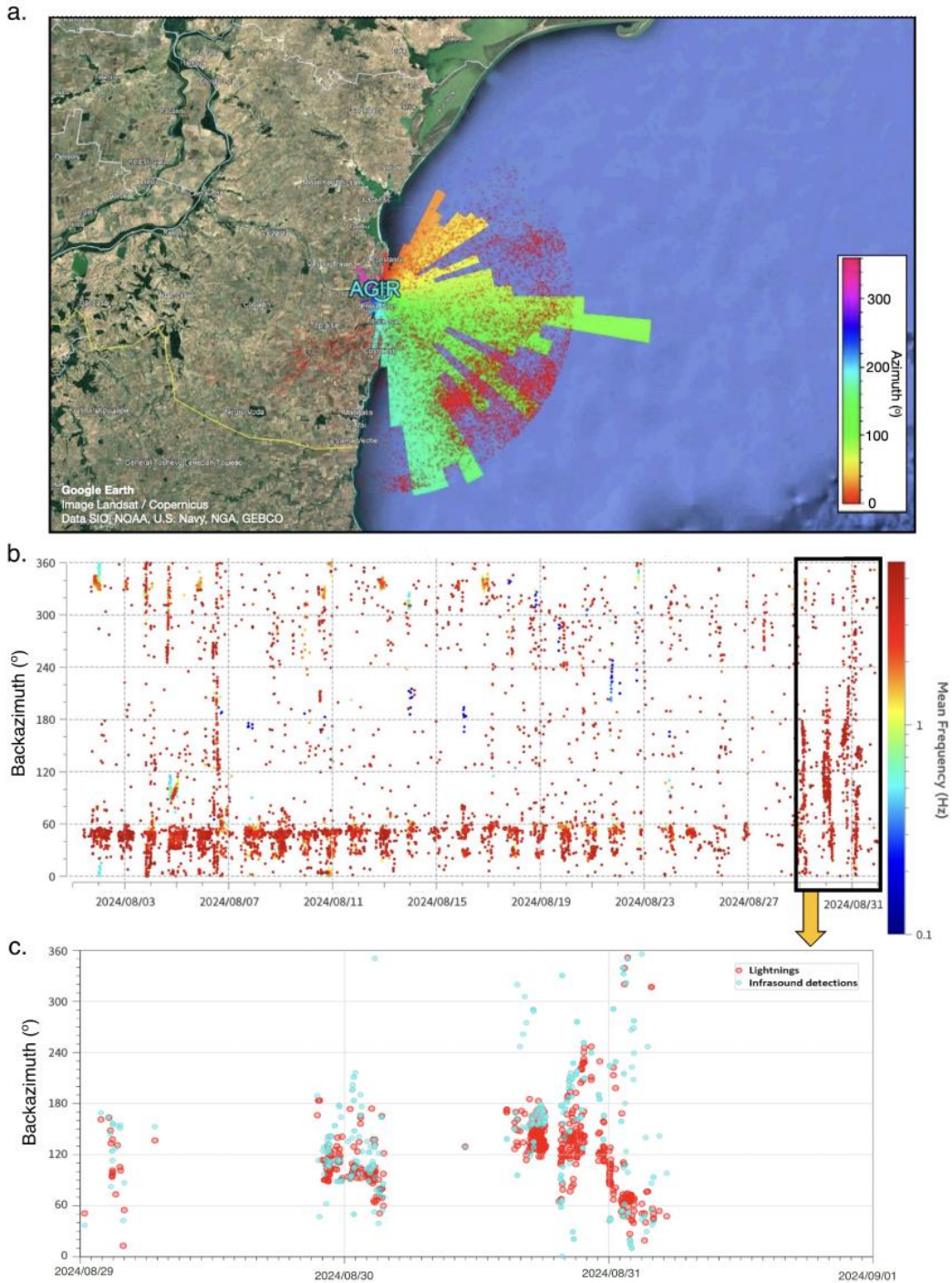
481

482 4.2.2 Array analysis and lightning detection

483 Using multiple sensors from the AGIR infrasound array with the PMCC algorithm allowed us to
484 isolate coherent infrasound signals and estimate their propagation parameters, such as backazimuth
485 and arrival times, across the sensor network. Nearly 11,000 lightning flashes were detected by the
486 MTG Lightning Imager within 50 km of the AGIR station during the Black Sea storm (Figure
487 10a), providing a dense reference set for comparison. Within the relevant 0.6-7 Hz frequency band,
488 approximately 1,100 infrasound detections were identified. These signals primarily consisted of
489 long-duration wave trains with frequent amplitude peaks and short-lived disturbances
490 characteristic of lightning-generated infrasound. Their dominant frequency was around 3 Hz, and
491 amplitudes ranged from 0.01 to 3.4 Pa (Figure 10b).

492 A subset of the infrasound detections could be confidently associated with individual lightning
493 discharges based on temporal alignment and backazimuth consistency. Overall, we were able to
494 associate 6.4% of lightning flashes with infrasound detections at AGIR (Figure 10c). This level of
495 correspondence is reasonable given that only a subset of lightning discharges radiate infrasound
496 efficiently and that propagation strongly depends on altitude, source geometry, and atmospheric
497 conditions. Nevertheless, these coincident detections demonstrate that lightning-generated
498 infrasound was clearly recorded during the storm and that the PMCC-derived acoustic signatures
499 provide valuable insight into the evolution of electrical activity and storm dynamics.

500 Anthropogenic noise sources, such as wind turbines (e.g., Jakobsen, 2005), industrial machinery
501 (Gastmeier and Howe, 2008), and road traffic (Grafkina et al., 2019), are well-documented
502 challenges for infrasound studies because they often generate persistent, periodic, or tonal signals
503 that can mask natural atmospheric phenomena. The AGIR infrasound array used here is located in
504 a semi-rural setting, distant from major roads and industrial facilities, which reduces the likelihood
505 of local anthropogenic contamination. Several independent lines of evidence indicate that such
506 contamination is negligible in this case study. First, the strongest infrasound signatures occurred
507 during night-time hours, when human activity is minimal. Second, both the clustering and PMCC
508 analyses identify transient signals with energy peaking around ~ 3 Hz, which contrasts sharply with
509 the more continuous or harmonic spectral patterns typically produced by anthropogenic sources.
510 Third, the temporal alignment of these acoustic signatures with independent observations of
511 lightning and precipitation provides strong confirmation that the detected infrasound variability is
512 storm-related rather than anthropogenic in origin.



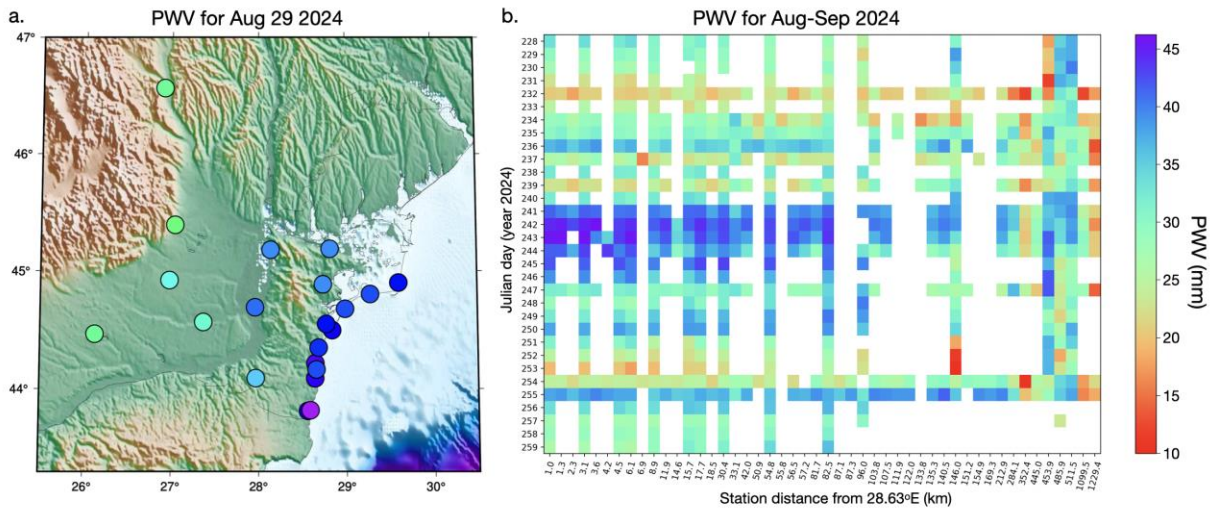
513

514 *Figure 10. a. Polar histogram of infrasound detections from the AGIR station, displayed with © Google*
 515 *Earth, along with the locations of lightning strikes detected by the MTG Lightning Imager system for the*
 516 *period from 29-31st of August 2024. The geographical position of the AGIR infrasound station is also*
 517 *shown on the map. b. diagram of high-frequency detections from the AGIR infrasound station between 1-*
 518 *31st of August 2024. c. Associations between events detected by the AGIR infrasound array and the MTG*
 519 *satellite database for 29-31st of August 2024.*

520 **4.3 GNSS-derived precipitable water vapor trends**

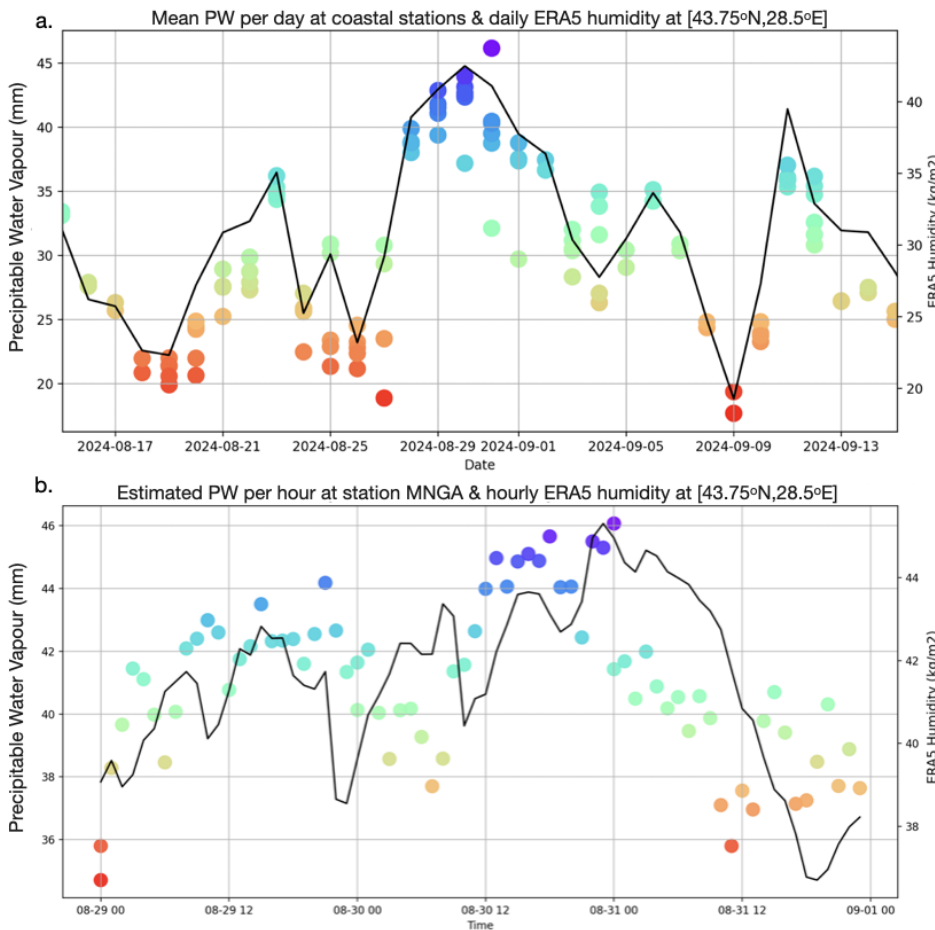
521 The analysis of daily GNSS-derived precipitable water vapor (Figure 11) reveals clear temporal
522 variations, with the highest PWV values consistently recorded on stormy days (>90040 mm per
523 day on DOY 240-243, i.e. August 27-30). Notably, the peak values occurred between DOY 241
524 and DOY 243 (Figure 11b), when the heaviest rainfall was observed (Figure 1). Coastal stations
525 showed extremely high PWV values (>95040 mm per day) compared to inland stations (<30800
526 mm per day), with a slight decrease in PWV away from the coast (Figure 11a). This spatial
527 distribution highlights the geographical gradient of atmospheric moisture, with the highest PWV
528 concentrations near coastal areas, also decreasing gradually toward the north away from the storm
529 peak. Interestingly, some inland stations (BUCU, PGNL, RMSR) recorded their peak PWV on
530 DOY 255, corresponding to the onset of the Boris storm, another significant extreme rainfall event
531 that swept through Central and Eastern Europe (Athanas et al., 2024).

532 Elevated PWV was observed as early as August 27th (Figure 12a), suggesting that the tropospheric
533 moisture loading began to increase several days before the onset of the rainfall. This accelerated
534 increase in PWV may act as an early indicator of a developing weather system.
535 Remarkably, although HARI, located inland, did not directly experience the extreme rainfall, it
536 exhibited similar PWV behavior to coastal stations, suggesting that GNSS stations, even outside
537 the immediate storm zones, can capture atmospheric signals indicative of intense precipitation.
538 This finding offers a valuable precedent, showing that PWV measurements at GNSS stations not
539 directly in the storm path can still provide critical insights into moisture dynamics at the
540 tropospheric level. The comparison with ERA5’s total-column water vapour further supports this
541 interpretation, as the broad temporal evolution of ERA5 humidity mirrors the GNSS-derived daily
542 PWV patterns, despite the inherently coarser resolution of the reanalysis data.



543
544 *Figure 11. a: Map of GNSS stations coloured as a function of PWV estimated for the 29th of August. b.*
545 *Daily PWV values for each station, plotted as a function of their longitudinal distance relative to 28.63°E.*
546 *the city of Constanța.*

547 Using the hourly PWV data, Figure 12b illustrates the evolution of water vapour at the MNGA
 548 station, which recorded the heaviest rainfall in the study area. Notably, MNGA also showed a rapid
 549 buildup of PWV, reaching values greater than 44 mm/hr just a few hours before the storm event.
 550 This rapid increase in PWV strongly suggests that the accumulation of atmospheric moisture may
 551 precede is a precursor to extreme weather events, such as intense rainfall and storms. This
 552 observation aligns with known atmospheric dynamics, where a significant increase in water vapor
 553 content precedes heavy precipitation, highlighting the potential usefulness of providing further
 554 evidence of the potential for GNSS-based PWV monitoring for studying pre-storm atmospheric
 555 moisture variability to serve as an early warning tool for extreme weather. The general rising trend
 556 toward the event is present in both GNSS-based and ERA5 reanalysis datasets, although some
 557 minor fluctuations are not matched. After the storm, the GNSS PWV drops sharply while ERA5
 558 maintains elevated values for several hours. These differences show that GNSS can resolve rapid,
 559 real-time atmospheric changes that may be blurred in large-scale weather model products.



560

561 *Figure 12. Comparison of GNSS-derived precipitable water vapor (coloured circles) with independent*
 562 *humidity data (black line) from ERA5's total column vertically integrated water vapor parameter. a. Daily*
 563 *Mean PWV values per day at selected GNSS stations (CONB, HARI, MNGA, MNGL, MNGM, TUZL)*
 564 *alongside daily averaged ERA5 humidity. b. Hourly Estimated PWV values per hour at the MNGA GNSS*
 565 *station compared with hourly ERA5 humidity at the 43.75°N, 28.5°E grid point. In both panels, GNSS data*

566 *points are represented by colored circles where the color scale corresponds to the PWV magnitude,*
567 *consistent with the vertical axis.*

568 **5. Discussion**

569 Storm evolution, in the meteorological sense, describes the sequence of processes from pre-storm
570 atmospheric moisture accumulation to convective initiation, peak rainfall, electrical activity, and
571 the associated marine response along coastal areas. The multi-sensor dataset used here captures
572 these different stages: GNSS-PWV documents the build-up of column water vapor before
573 convective onset, infrasound detects lightning-generated acoustic waves and pressure disturbances
574 during the mature convective phase, high-frequency seismic noise reflects the timing and spatial
575 progression of intense rainfall at the surface, microseisms respond to storm-driven changes in sea
576 state, and ERA5/MTG provide the mesoscale structure that ties these geophysical signals together.
577 By observing the same storm through these complementary physical pathways, we can outline a
578 more detailed picture of how the storm developed, intensified, and decayed than is possible from
579 individual datasets.

580 The integration of infrasound, seismic, and GNSS data in monitoring the extreme storm event over
581 the Black Sea provides valuable insights into the dynamics of storm behavior and ~~demonstrates~~
582 *illustrates* the potential of repurposing non-conventional sensors for meteorological analysis.
583 Infrasound data, for instance, revealed a clear acoustic signature of lightning activity, with signals
584 detected in the range of 0.6 to 7 Hz corresponding to electrical discharges. The high frequency of
585 infrasound detections (around 1,100) ~~supports its utility as a reliable tool~~ *suggests that it may*
586 *provide useful information* for tracking storm-related phenomena, particularly lightning, which is
587 difficult to capture with traditional methods. However, the signals did not always perfectly align
588 with lightning strikes, indicating that other factors, such as the movement of storm systems or
589 variations in atmospheric conditions, may influence infrasound signatures. This suggests that
590 refining the correlation between infrasound signals and lightning activity could be an avenue for
591 future research, particularly in cases of sparse lightning or in remote regions.

592 Seismic data alone also showed a strong connection between high-frequency seismic noise and
593 heavy rainfall, supporting previous studies that linked seismic signals to rainfall intensity. The
594 distinction between high-frequency and low-frequency seismic noise is particularly noteworthy.
595 Increases in high-frequency seismic noise occurred during intense precipitation, while low-
596 frequency signals were associated with wave height and storm-driven winds. This suggests that
597 different seismic frequencies capture distinct storm dynamics, with high-frequency signals
598 reflecting localized rainfall impacts and low-frequency signals tied to broader atmospheric and
599 oceanic interactions. This dual-frequency approach provides a more nuanced interpretation of
600 seismic data in storm monitoring, highlighting its complexity.

601 A key finding of this study is that K-means clustering of multiple acoustic features, including
602 spectral centroids, roll-off, flux, and zero-crossing rate, effectively segmented the infrasound
603 record into distinct storm phases. This approach proved more robust than relying on any single
604 feature, as the combination captured the complex, evolving nature of the storm's acoustic signature.
605 For instance, the identified clusters delineated periods of intense precipitation, elevated
606 background acoustic levels, and calm intervals, providing a data-driven overview of the storm's
607 progression. The fact that these acoustically defined phases align with independent meteorological

608 observations, such as rainfall peaks, confirms that the infrasound signal variability is a direct
609 response to the storm's atmospheric dynamics.

610 Furthermore, the observed spectral similarity between the infrasound signals and high-frequency
611 seismic envelopes suggests a coupled seismo-acoustic response to the storm. This implies that the
612 same atmospheric forcing, such as pressure fluctuations from rainfall and wind, generates
613 complementary signals in the atmosphere (infrasound) and the ground (seismic waves). Our
614 findings are consistent with other studies of intense weather systems, where coupled microbarom-
615 microseism signals have been shown to track storm structure and evolution (e.g., Butler & Aucan,
616 2018; Smirnov, 2021). The coherent acoustic and seismic responses to atmospheric-oceanic
617 pressures, as also documented in Distributed Acoustic Sensing studies (Taweessintananon et al.,
618 2023) and surf studies (Francoeur et al., 2025), reinforce the interpretation of a shared source
619 mechanism. Therefore, a major and logical next step is to move beyond analyzing these datasets
620 in parallel and to perform joint clustering of seismo-acoustic data (e.g. Floroiu et al., 2025). Such
621 an integrated approach could unlock a more comprehensive, multi-physics understanding of storm
622 dynamics by simultaneously characterizing the coupled atmospheric and ground-borne wavefields.

623 The temporal variations observed in GNSS-derived integrated precipitable water vapor provide
624 valuable insights into atmospheric moisture dynamics before extreme weather events. The
625 pronounced increase in PWV, particularly in the days leading up to and during the storm, supports
626 the link between elevated atmospheric water vapor and precipitation. Notably, the PWV buildup
627 starting roughly three days before the extreme rainfall suggests that rising moisture levels in the
628 troposphere ~~were observed prior to the~~ ~~can serve as an early indicator of impending~~ intense
629 precipitation ~~in this event~~. Even stations located up to 130 km inland, such as HAR1, recorded
630 similar PWV trends, indicating that GNSS stations outside direct storm zones can still provide
631 crucial atmospheric data. Hourly PWV trends further revealed a rapid increase several hours before
632 precipitation, with values exceeding 44 mm/hr, highlighting the accumulation of moisture just
633 before heavy rainfall. These findings align with the notion that increasing atmospheric moisture
634 acts as a precursor to intense precipitation, highlighting the potential of GNSS-based PWV
635 monitoring ~~as a real-time tool~~ for tracking moisture and understanding short-term atmospheric
636 fluctuations.

637 The integration of GNSS, infrasound, and seismic data provides a more comprehensive
638 understanding of storm dynamics than any single data source alone. The synergy between these
639 diverse sensor types allows for the detection of atmospheric moisture, lightning activity, rainfall-
640 induced seismic signals, and storm-driven oceanic interactions. Future research should focus on
641 refining unsupervised learning algorithms for infrasound and seismic signal classification,
642 optimizing joint clustering techniques, and improving the integration of these data sources to
643 enhance storm forecasting and early-warning systems. ~~We believe~~ ~~This case study suggests that~~
644 this multi-sensor approach ~~may help~~ ~~holds promise for~~ ~~improving~~ our ability to predict extreme
645 weather events, understand their impacts, and mitigate associated risks.

646 **6. Conclusions**

647 This study presents a comprehensive analysis of a record-breaking storm over the Black Sea, using
648 a combination of GNSS, infrasound, and seismic data to capture the dynamics of extreme weather
649 events. Our findings underscore the power of multi-sensor networks in enhancing the

650 understanding of storm behavior, particularly in the context of atmospheric moisture, lightning
651 activity, and storm-induced seismic signals. GNSS-derived integrated precipitable water vapor
652 indicates a clear buildup of atmospheric moisture hours before the onset of heavy rainfall,
653 providing valuable insights into the lead-up to extreme precipitation events. Infrasound and
654 seismic data further complemented this analysis, with infrasound [providing useful observations of](#)
655 [serving as a reliable tool for tracking](#) lightning activity and seismic data revealing the link between
656 rainfall intensity and high-frequency seismic noise.

657 The storm analysed here represents an exceptional meteorological event and one of the most
658 intense storms recorded in the region in recent years. An attribution analysis using the ClimaMeter
659 framework (Antonescu et al., 2024) identified a detectable anthropogenic climate change signal
660 associated with this event, placing it within the broader context of intensifying extremes in a
661 [warming climate](#). ~~we analyzed is not only a significant meteorological event but also serves as a~~
662 ~~powerful example of how climate change may be influencing the frequency and intensity of~~
663 ~~extreme weather phenomena. Record-breaking storms like this are increasingly being recognized~~
664 ~~as evidence of shifting atmospheric conditions, driven by global climate change.~~ The integration
665 of GNSS, infrasound, and seismic data provides a more nuanced and holistic view of storm
666 dynamics, highlighting the need for advanced monitoring systems to predict and respond to such
667 extreme events. Looking forward, [such multi-sensor approaches may support future developments](#)
668 [in integrated environmental monitoring and research into early-warning capabilities, ultimately](#)
669 [contributing to improved understanding and characterization of high-impact atmospheric events.](#)
670 ~~the combination of these innovative tools holds great potential for improving early warning~~
671 ~~systems, enhancing storm forecasting, and better understanding the impacts of climate change on~~
672 ~~atmospheric and oceanic processes.~~

673 7. Code availability

674 Seismic data were processed with the open-source python framework for seismology Obspy
675 (Beyreuther et al., 2010). Infrasound data was processed with the WinPMCC software (Le Pichon
676 et al., 2010) developed by CEA/DASE (French Atomic Energy Commission, Environmental
677 Assessment and Monitoring Department) and open-source Python libraries for signal processing.
678 Some of the figures were made with GMT (Generic Mapping Tools, Wessel et al., 2019). The
679 GNSS data was processed using Gamit/Globk (Herring et al., 2020) developed by Massachusetts
680 Institute of Technology (<http://www-gpsg.mit.edu/gg/>).

681 8. Data availability

682 [Processed infrasound, seismic, and GNSS-derived integrated water vapour data can be visualized](#)
683 [and accessed via the INFP monitoring platforms: <https://infp.ro/dashboard-reactive.php> and](#)
684 <https://reactive.infp.ro/events/>. Seismic data are part of the Romanian National Seismic Network
685 maintained by the National institute for Earth Physics (NIEP, www.infp.ro) and are freely
686 available in the miniseed format via EIDA (European Integrated Data Archive,
687 <https://www.orfeus-eu.org/data/eida/>). GNSS data are available for download from NIEP
688 (<http://gps.infp.ro/#/download>) and are provided in the standardized RINEX v2 format, with 24-
689 hour files sampled at 30-second intervals. Infrasound data at AGIR are available to download from
690 NIEP via FDSN dataselect web service. Hourly hydro-meteorological data were obtained from the
691 Copernicus Climate Change Service, Climate Data Store (<https://doi.org/10.24381/cds.bd0915c6>),

692 ERA5 dataset (Hersbach et al., 2023). Limited wind and precipitation data were downloaded from
693 the National Meteorological Agency from <https://www.meteoromania.ro/grafice/> (accessed on
694 13.09.2024) and from https://www.meteoromania.ro/clim/caracterizare-lunara/cc_2024_08.html
695 (accessed on 10.11.2025), respectively. Lightning data came from Meteosat Third Generation
696 Lightning Imager operated by EUMETSAT (The European Organisation for the Exploitation of
697 Meteorological Satellites, <https://www.eumetsat.int/>).

698

699 **9. Author contribution**

700 **Laura Petrescu:** Conceptualization, Methodology, Software, Formal analysis, Data Curation,
701 Writing-Original Draft, Visualization; **Bogdan Antonescu:** Conceptualization, Writing-Review &
702 Editing, Visualization; **Sorin Nistor:** Software, Formal Analysis, Data curation, Visualisation,
703 Writing-Review & Editing; **Iustin Floroiu:** Methodology, Software, Formal analysis, Data
704 Curation, Writing-Original Draft, Visualization; **Dragoş Ene:** Software, Formal analysis, Data
705 Curation, Writing-Review & Editing; **Daniela Ghica:** Software, Formal analysis, Data Curation;
706 **Constantin Ionescu:** Funding Acquisition, Resources, Project administration; **Andrei Anghel:**
707 Methodology, Supervision; **Mihai Datcu:** Methodology, Supervision, Funding Acquisition,
708 Resources, Project administration.

709 **10. Acknowledgments**

710 We would like to thank the technicians and staff at NIEP for their support in installing,
711 maintaining, and ensuring the proper functioning of the equipment used in this study. Additionally,
712 we appreciate the efforts of those involved in data formatting and preparation (Cristian Neagoe,
713 Eduard Nastase, Victorin Toader) which were essential for this work. We also thank the two
714 anonymous reviewers for their valuable feedback, which helped improve the manuscript.

715 **11. Financial support:**

716 This work was carried out in the framework of the “Competence Center for Climate Change Digital
717 Twin for Earth forecasts and societal redressment” Project PNRR- DTEClimate nr.
718 760008/31.12.2023, subproject Reactive “The Research center for climate change due to natural
719 disasters and extreme weather events”, supported by the Ministry of Research, Innovation and
720 Digitalization of Romania.

721 **12. References**

722 Antonescu, B., Dafis, S., & Faranda, D.: Changes in precipitation patterns driving August 2024
723 Romania floods mostly driven by human-driven climate change. *ClimaMeter, Institut Pierre*
724 *Simon Laplace, CNRS*. <https://doi.org/10.5281/zenodo.14056214>, 2018.

725 Ardhuin, F., Gualtieri, L., Stutzmann, E., Nakata, N. and Fichtner, A.: Physics of ambient noise
726 generation by ocean waves. In *Seismic ambient noise*, Eds: Nakata, N., Gualtieri, L., Fichtner, A.
727 Cambridge University Press, 69-108, <https://doi.org/10.1017/9781108264808.005>, 2019.

- 728 Assink, J. D., Evers, L. G., Holleman, I., and Paulssen, H.: Characterization of infrasound from
729 lightning, *Geophysical Research Letters*, 35, L15802, <https://doi.org/10.1029/2008GL034193>,
730 2008.
- 731 Aster, R.C., McNamara, D.E. & Bromirski, P.D.: Multidecadal climate-induced variability in
732 microseisms. *Seismological Research Letters*, 79(2), 194-202,
733 <https://doi.org/10.1785/gssrl.79.2.194>, 2008.
- 734 Aster, R.C., Ringler, A.T., Anthony, R.E., & Lee, T.A.: Increasing ocean wave energy observed
735 in Earth's seismic wavefield since the late 20th century. *Nature Communications*, 14(1), 6984,
736 <https://doi.org/10.1038/s41467-023-42673-w>, 2023.
- 737 Athanase, M., Sánchez-Benítez, A., Monfort, E., Jung, T. and Goessling, H.F.: How climate
738 change intensified storm Boris' extreme rainfall, revealed by near-real-time storylines.
739 *Communications Earth & Environment*, 5(1), 676, <https://doi.org/10.1038/s43247-024-01847-0>,
740 2024.
- 741 Awange, J.L.: Environmental monitoring using GNSS: Global navigation satellite systems,
742 Springer, Heidelberg, <https://doi.org/10.1007/978-3-540-88256-5>, 2012.
- 743 Beyreuther, M., Barsch, R., Krischer, L., Megies, T., Behr, Y. and Wassermann, J.: ObsPy: A
744 Python toolbox for seismology. *Seismological Research Letters*, 81(3), 530-533,
745 <https://doi.org/10.1785/gssrl.81.3.530>, 2010.
- 746 Bengtsson, L., Hodges, K.I. and Roeckner, E.: Storm tracks and climate change. *Journal of*
747 *climate*, 19(15), 3518-3543, <https://doi.org/10.1175/JCLI3815.1>, 2006.
- 748 Bližňák, V. and Sokol, Z.: First validation of the Lightning Imager aboard Meteosat Third
749 Generation satellite with Earth Networks Total Lightning Network. *International Journal of*
750 *Applied Earth Observation and Geoinformation*, 147, 105205,
751 <https://doi.org/10.1016/j.jag.2026.105205>, 2026.
- 752 Bollinger, L., Perrier, F., Avouac, J.P., Sapkota, S., Gautam, U., Tiwari, D.R.: Seasonal
753 modulation of seismicity in the Himalaya of Nepal, *Geophysical Research Letters*, 34(8),
754 <https://doi.org/10.1029/2006GL029192>, 2007.
- 755 Bondár, I., Šindelářová, T., Ghica, D., Mitterbauer, U., Liaschuk, A., Baše, J., Chum, J., Czanik,
756 C., Ionescu, C., Neagoe, C. and Pásztor, M.: Central and Eastern European Infrasound Network:
757 contribution to infrasound monitoring, *Geophysical Journal International*, 230(1), 565-579,
758 <https://doi.org/10.1093/gji/ggac066>, 2022.
- 759 Borzì, A.M., Minio, V., Cannavò, F., Cavallaro, A., D'Amico, S., Gauci, A., De Plaen, R., Lecocq,
760 T., Nardone, G., Orasi, A., Picone, M., Cannata, A.: Monitoring extreme meteo-marine events in

761 the Mediterranean area using the microseism (Medicane Apollo case study). *Scientific Reports*,
762 12(1), <https://doi.org/10.1038/s41598-022-25395-9>, 2022.

763 Bosy, J., Kaplon, J., Rohm, W., Sierny, J. and Hadas, T.: Near real-time estimation of water vapour
764 in the troposphere using ground GNSS and the meteorological data, *Annales Geophysicae*, 30,
765 1379–1391, <https://doi.org/10.5194/angeo-30-1379-2012>, 2012.

766 Brachet, N., Brown, D., Le Bras, R., Cansi, Y., Mialle, P., Coyne, J.: Monitoring the Earth’s
767 Atmosphere with the Global IMS Infrasound Network, in: *Infrasound Monitoring for Atmospheric*
768 *Studies*, edited by: Le Pichon, A., Blanc, E., Hauchecorne, A. , Springer, Dordrecht,
769 https://doi.org/10.1007/978-1-4020-9508-5_3, 2010.

770 Bromirski, P.D. and Duennebier, F.K.: The near-coastal microseism spectrum: Spatial and
771 temporal wave climate relationships. *Journal of Geophysical Research: Solid Earth*, 107(B8), ESE
772 5-1-ESE 5-20, <https://doi.org/10.1029/2001JB000265>, 2002.

773 Bruyninx, C., Habrich, H., Söhne, W., Kenyeres, A., Stangl, G. and Völksen, C.: Enhancement of
774 the EUREF permanent network services and products, in: *Proceedings of the International*
775 *Association of Geodesy, Symposium on Geodesy for Planet Earth, Buenos Aires, Argentina, 31*
776 *August-4 September 2009, 27-34*, 2012.

777 Burtin, A., Hovius, N. and Turowski, J.M.: Seismic monitoring of torrential and fluvial processes.
778 *Earth Surface Dynamics*, 4(2), 285-307, <https://doi.org/10.5194/esurf-4-285-2016>, 2016.

779 Butler, R. and Aucan, J.: Multisensor, microseismic observations of a hurricane transit near the
780 ALOHA cabled observatory. *Journal of Geophysical Research: Solid Earth*, 123(4), 3027-3046,
781 2018.

782 Campus, P. and Christie, D.R.: Worldwide observations of infrasonic waves, in: *Infrasound*
783 *monitoring for atmospheric studies*, edited by: Le Pichon, A., Blanc, E., Hauchecorne, A.,
784 Springer, Dordrecht, Netherlands, 185-234, https://doi.org/10.1007/978-1-4020-9508-5_6, 2009.

785 Cansi, Y. and Pichon, A.L.: Infrasound event detection using the progressive multi-channel
786 correlation algorithm, in: *Handbook of signal processing in acoustics.*, edited by: Havelock, D.,
787 Kuwano, S., Vorländer, M., Springer, New York, 1425-1435, https://doi.org/10.1007/978-0-387-30441-0_77, 2008.

789 Coates, A. and Ng, A.Y.: Learning feature representations with k-means. In *Neural Networks:*
790 *Tricks of the Trade: Second Edition (561-580)*. Berlin, Heidelberg: Springer Berlin Heidelberg,
791 2012.

792 Coviello, V., Palo, M., Adirosi, E. and Picozzi, M.: Seismic signature of an extreme hydro-
793 meteorological event in Italy, *Natural Hazards*, 1(1), 17, [https://doi.org/10.1038/s44304-024-](https://doi.org/10.1038/s44304-024-00018-7)
794 [00018-7](https://doi.org/10.1038/s44304-024-00018-7), 2024.

- 795 Diaz, J., Ruiz, M., Udina, M., Polls, F., Martí, D., Bech, J.: Monitoring storm evolution using a
796 high-density seismic network, *Scientific Reports*, 13(1), [https://doi.org/10.1038/s41598-023-](https://doi.org/10.1038/s41598-023-28902-8)
797 28902-8, 2023.
- 798 Díaz, J., Ruiz, M., Sánchez-Pastor, P.S. and Romero, P.: Urban seismology: On the origin of earth
799 vibrations within a city. *Scientific reports*, 7(1), 15296, 2017.
- 800 Dimitriu, R.G., Stanciu, I.M., Barbu M.-B., Dobrev, N., Dumitru, P.: First results on the western
801 Black Sea coast geodynamics resulted from GeoPontica permanent GNSS stations network data
802 processing, in: Proceedings of the 17th International Multidisciplinary Scientific GeoConference
803 SGEM, Albena, Bulgaria August 2017, 17(11), 149-157, 2017.
- 804 Dullaart, J.C., Muis, S., Bloemendaal, N. and Aerts, J.C.: Advancing global storm surge modelling
805 using the new ERA5 climate reanalysis. *Climate Dynamics*, 54(1), 1007-1021, 2020.
- 806 Ebeling, C.W.: Inferring Ocean Storm Characteristics from Ambient Seismic Noise. A Historical
807 Perspective, *Advances in Geophysics*, 53, 1-33. [https://doi.org/10.1016/B978-0-12-380938-](https://doi.org/10.1016/B978-0-12-380938-4.00001-X)
808 4.00001-X, 2012.
- 809 [Enno, S.-E., Viticchie, B., Navia, D. and Grandell, J.: Meteosat-12 Lightning Imager: first year of
810 observations and the main performance characteristics, in: 12th European Conference on Severe
811 Storms, 08 August 2025, <https://doi.org/10.5194/ecss2025-152>, 2025.](#)
- 812 Faranda, D., Messori, G., Coppola, E., Alberti, T., Vrac, M., Pons, F., Yiou, P., Saint Lu, M., Hisi,
813 A. N. S., Brockmann, P., Dafis, S., Mengaldo, G., and Vautard, R.: ClimaMeter: contextualizing
814 extreme weather in a changing climate, *Weather Climate Dynamics*, 5, 959-983,
815 <https://doi.org/10.5194/wcd-5-959-2024>, 2024.
- 816 Floroiu, I., Anghel, A., Petrescu, L. and Datcu, M.: Clustering and Feature-Based Similarity
817 Retrieval of Infrasound Events during Two Storms in Constanța, Romania, *International
818 Conference on Machine Intelligence for GeoAnalytics and Remote Sensing (MIGARS)*, Bucharest,
819 Romania, 2025, 1-4, <https://doi.org/10.1109/MIGARS67156.2025.11231952>, 2025.
- 820 Francoeur, J.W., Matoza, R.S., Ortiz, H.D. and De Negri, R.: Identification of transient seismo-
821 acoustic signals from crashing ocean waves: template matching and location of discrete surf
822 events. *Geophysical Journal International*, 243(2), ggaf317, 2025.
- 823 Garcés, M.A.: On infrasound standards, part 1 time, frequency, and energy scaling. *InfraMatics*,
824 2(2),13–35, <https://doi.org/10.4236/inframatics.2013.22002>, 2013.
- 825 Gastmeier, W.J. and Howe, B.: Recent studies of infrasound from industrial sources. *Canadian
826 Acoustics*, 36(3), 58-59, 2008.
- 827 Grafkina, M.V., Nyunin, B.N. and Sviridova, E.Y: Environmental monitoring and simulation of
828 infrasound generating mechanism of traffic flow. *Journal of Ecological Engineering*, 20(7),
829 2019.

830 Grevemeyer, I., Herber, R. and Essen, H.H.: Microseismological evidence for a changing wave
831 climate in the northeast Atlantic Ocean. *Nature*, 408(6810), 349-352,
832 <https://doi.org/10.1038/35042558>, 2000.

833 Groos, J.C. and Ritter, J.R.R.: Time domain classification and quantification of seismic noise in
834 an urban environment. *Geophysical Journal International*, 179(2), pp.1213-1231, 2009.

835 Gualtieri, L., Camargo, S.J., Pascale, S., Pons, F.M.E., & Ekström, G.: The persistent signature of
836 tropical cyclones in ambient seismic noise, *Earth and Planetary Science Letters*, 484, 287-294.
837 <https://doi.org/10.1016/j.epsl.2017.12.026>, 2018.

838 Guerova, G., Jones, J., Douša, J., Dick, G., de Haan, S., Pottiaux, E., Bock, O., Pacione, R.,
839 Elgered, G., Vedel, H. and Bender, M.: Review of the state of the art and future prospects of the
840 ground-based GNSS meteorology in Europe, *Atmospheric Measurement Techniques*, 9(11),
841 5385–5406, <https://doi.org/10.5194/amt-9-5385-2016>, 2016.

842 Herring, T., King, R., Floyd, M., McClusky, S.: GAMIT Reference Manual GPS Analysis at MIT
843 Release 10.7. GAMIT/GLOBK, 2020.

844 Hersbach, H., Bell, B., Berrisford, P., Hirahara, S., Horányi, A., Muñoz-Sabater, J., Nicolas, J.,
845 Peubey, C., Radu, R., Schepers, D. and Simmons, A.: The ERA5 global reanalysis, *Quarterly*
846 *Journal of the Royal Meteorological Society*, 146(730), 1999-2049, 2020.

847 Hersbach, H., Bell, B., Berrisford, P., Biavati, G., Horányi, A., Muñoz Sabater, J., Nicolas, J.,
848 Peubey, C., Radu, R., Rozum, I., Schepers, D., Simmons, A., Soci, C., Dee, D., Thépaut, J.-N.:
849 ERA5 hourly data on single levels from 1940 to present. Copernicus Climate Change Service
850 (C3S) Climate Data Store (CDS), <https://doi.org/10.24381/cds.adbb2d47>, 2023.

851 Holmlund, K., Grandell, J., Schmetz, J., Stuhlmann, R., Bojkov, B., Munro, R., Lekouara, M.,
852 Coppens, D., Viticchie, B., August, T. and Theodore, B.: Meteosat Third Generation (MTG):
853 Continuation and innovation of observations from geostationary orbit, *Bulletin of the American*
854 *Meteorological Society*, 102(5), E990-E1015, <https://doi.org/10.1175/BAMS-D-19-0304.1>, 2021.

855 Hua, J., Wu, M., Mulholland, J.P., Neelin, J.D., Tsai, V.C. and Trugman, D.T.: High-resolution
856 precipitation monitoring with a dense seismic nodal array. *Scientific Reports*, 13(1), 11450,
857 <https://doi.org/10.1038/s41598-023-38008-w>, 2023.

858 Hupe, P., Ceranna, L., Pilger, C., de Carlo, M., Le Pichon, A., Kaifler, B. and Rapp, M.: Assessing
859 middle atmosphere weather models using infrasound detections from microbaroms. *Geophysical*
860 *Journal International*, 216(3), 1761-1767, <https://doi.org/10.1093/gji/ggy520>, 2019.

861 Hupe, P., Ceranna, L., Le Pichon, A., Matoza, R.S. and Mialle, P.: International Monitoring
862 System infrasound data products for atmospheric studies and civilian applications. *Earth System*
863 *Science Data Discussions*, 14, 4201–4230, <https://doi.org/10.5194/essd-14-4201-2022>, 2022.

864 Iliescu, A. I., Rus, T., Danciu, V., Moldoveanu, C., & Ilie, A.: Current situation of GNSS networks
865 in Romania, *Bulletin of University of Agricultural Sciences and Veterinary Medicine Cluj-Napoca.*
866 *Horticulture*, 76(2), 2019.

867 Jakobsen, J.: Infrasound emission from wind turbines. *Journal of low frequency noise, vibration*
868 *and active control*, 24(3), 145-155, 2005.

869 Jiao, D., Xu, N., Yang, F. and Xu, K.: Evaluation of spatial-temporal variation performance of
870 ERA5 precipitation data in China. *Scientific Reports*, 11(1), 17956, 2021.

871 Johnston, G., Riddell, A. and Hausler, G.: The international GNSS service, in: Springer handbook
872 of global navigation satellite systems, edited by: Teunissen, P.J. and Montenbruck, O., Springer,
873 Cham, Switzerland, 967-982, https://doi.org/10.1007/978-3-319-42928-1_33, 2017.

874 Jones, J., Guerova, G., Douša, J., Dick, G., de Haan, S., Pottiaux, E., Bock, O., Pacione, R. and
875 Van Malderen, R.: Advanced GNSS tropospheric products for monitoring severe weather events
876 and climate, COST Action ES1206 Final Action Dissemination Report, 563, 2020.

877 Karabatić, A., Weber, R. and Haiden, T.: Near real-time estimation of tropospheric water vapour
878 content from ground based GNSS data and its potential contribution to weather now-casting in
879 Austria, *Advances in Space Research*, 47(10), 1691–1703,
880 <https://doi.org/10.1016/j.asr.2010.10.028>, 2011.

881 Kober, K. and Tafferner, A.: Tracking and nowcasting of convective cells using remote sensing
882 data from radar and satellite, *Meteorologische Zeitschrift*, 1(18), 75-84,
883 <https://doi.org/10.1127/0941-2948/2009/359>, 2009.

884 Koper, K.D. & Burlacu, R.: The fine structure of double-frequency microseisms recorded by
885 seismometers in North America. *Journal of Geophysical Research: Solid Earth*, 120(3), 1677-
886 1691. <https://doi.org/10.1002/2014JB011820>, 2015.

887 [Kokou, P.: Status of the MTG-II Lightning Imager commissioning activities, in: EUMETSAT](#)
888 [Conference 2023, 1-C GEO – MTG, Malmö, Sweden, 12 September 2023, 2023.](#)

889 Landès, M., Ceranna, L., Le Pichon, A. and Matoza, R.S.: Localization of microbarom sources
890 using the IMS infrasound network. *Journal of Geophysical Research: Atmospheres*, 117(D6),
891 <https://doi.org/10.1029/2011JD016684>, 2012.

892 Landskron, D., Böhm, J.: VMF3/GPT3: refined discrete and empirical troposphere mapping
893 functions, *Journal of Geodesy*, 92, 349–360, <https://doi.org/10.1007/s00190-017-1066-2>, 2018.

894 Li, L., Boué, P., Retailleau, L., & Campillo, M.: Spatiotemporal Correlation Analysis of Noise-
895 Derived Seismic Body Waves With Ocean Wave Climate and Microseism Sources, *Geochemistry,*
896 *Geophysics, Geosystems*, 21(9), <https://doi.org/10.1029/2020GC009112>, 2020.

897 Listowski, C., Forestier, E., Dafis, S., Farges, T., De Carlo, M., Grimaldi, F., Le Pichon, A.,
898 Vergoz, J., Heinrich, P. and Claud, C.: Remote monitoring of Mediterranean hurricanes using
899 infrasound, *Remote Sensing*, 14(23), 6162, <https://doi.org/10.3390/rs14236162>, 2022.

900 MacQueen, J.: Some methods for classification and analysis of multivariate observations, in:
901 Proceedings of the Fifth Berkeley Symposium on Mathematical Statistics and Probability,
902 Berkeley, California, January 1967, 5, 281-298, 1967.

903 Marut, G., Hadas, T., Kaplon, J., Trzcina, E. and Rohm, W.: Monitoring the water vapor content
904 at high spatio-temporal resolution using a network of low-cost multi-GNSS receivers, *IEEE*
905 *Transactions on Geoscience and Remote Sensing*, 60, 1-14,
906 <https://doi.org/10.1109/TGRS.2022.3226631>, 2022.

907 Pásztor, M., Czanik, C. and Bondár, I.: A single array approach for infrasound signal
908 discrimination from quarry blasts via machine learning, *Remote Sensing*, 15(6), 1657,
909 <https://doi.org/10.3390/rs15061657>, 2023.

910 Le Pichon, A., Matoza, R., Brachet, N. and Cansi, Y.: Recent enhancements of the PMCC
911 infrasound signal detector. *Inframatics*, 26, 5-8, 2010.

912 Price, I., Sanchez-Gonzalez, A., Alet, F., Andersson, T.R., El-Kadi, A., Masters, D., Ewalds, T.,
913 Stott, J., Mohamed, S., Battaglia, P. and Lam, R.: Probabilistic weather forecasting with machine
914 learning. *Nature*, 637(8044), 84-90, 2025

915 Priego, E., Jones, J., Porres, M.J. and Seco, A.: Monitoring water vapour with GNSS during a
916 heavy rainfall event in the Spanish Mediterranean area, *Geomatics, Natural Hazards and Risk*,
917 8(2), 282–294, <https://doi.org/10.1080/19475705.2016.1201150>, 2017.

918 Retailleau, L. & Gualtieri, L.: Multi-phase seismic source imprint of tropical cyclones, *Nature*
919 *Communications*, 12(1), <https://doi.org/10.1038/s41467-021-22231-y>, 2021.

920 Rindraharisaona, E.J., Réchou, A., Fontaine, F.R., Barruol, G., Stamenoff, P., Boudevillain, B.,
921 Rigaud-Louise, F. and Delcher, E.: Seismic signature of rain and wind inferred from seismic data,
922 *Earth and Space Science*, 9(10), p.e2022EA002328, 2022.

923 Šindelářová, J., Chum, J., Skripnikova, K., and Base, J.: Atmospheric infrasound observed during
924 intense convective storms on 9–10 July 2011, *Journal of Atmospheric and Solar-Terrestrial*
925 *Physics*, 122, 66–74, <https://doi.org/10.1016/j.jastp.2014.10.014>, 2015.

926 Šindelářová, T., De Carlo, M., Czanik, C., Ghica, D., Kozubek, M., Podolská, K., Baše, J., Chum,
927 J., and Mitterbauer, U.: Infrasound signature of the post-tropical storm Ophelia at the Central and
928 Eastern European Infrasound Network, *Journal of Atmospheric and Solar-Terrestrial Physics*, 217,
929 105603, <https://doi.org/10.1016/j.jastp.2021.105603>, 2021.

- 930 Smirnov, A., De Carlo, M., Le Pichon, A., Shapiro, N.M. and Kulichkov, S.: Characterizing the
931 oceanic ambient noise as recorded by the dense seismo-acoustic Kazakh network. *Solid Earth*,
932 *12*(2), 503-520, 2021.
- 933 Soci, C., Hersbach, H., Simmons, A., Poli, P., Bell, B., Berrisford, P., Horányi, A., Muñoz-Sabater,
934 J., Nicolas, J., Radu, R. and Schepers: The ERA5 global reanalysis from 1940 to 2022. *Quarterly*
935 *Journal of the Royal Meteorological Society*, *150*(764), 4014-4048, 2024.
- 936 Sokol, Z., Szturc, J., Orellana-Alvear, J., Popova, J., Jurczyk, A. and Célleri, R.: The role of
937 weather radar in rainfall estimation and its application in meteorological and hydrological
938 modelling—A review, *Remote Sensing*, *13*(3), 351, 2021.
- 939 Stopa, J.E., Cheung, K.F., Garcés, M.A. and Badger, N.: Atmospheric infrasound from nonlinear
940 wave interactions during Hurricanes Felicia and Neki of 2009, *Journal of Geophysical Research:*
941 *Oceans*, *117*(C12), <https://doi.org/10.1029/2012JC008257>, 2012
- 942 Stott, P.: How climate change affects extreme weather events. *Science*, *352*(6293), 1517-1518,
943 <https://doi.org/10.1126/science.aaf7271>, 2016.
- 944 Tanimoto, T. & Anderson, A.: Seismic noise between 0.003 Hz and 1.0 Hz and its classification,
945 *Progress in Earth and Planetary Science*, *10*(1), <https://doi.org/10.1186/s40645-023-00587-7>,
946 2023.
- 947 Taweessintananon, K., Landrø, M., Potter, J.R., Johansen, S.E., Rørstadbotnen, R.A., Bouffaut, L.,
948 Kriesell, H.J., Brenne, J.K., Haukanes, A., Schjelderup, O. and Storvik, F.: Distributed acoustic
949 sensing of ocean-bottom seismo-acoustics and distant storms: A case study from Svalbard,
950 Norway. *Geophysics*, *88*(3), B135-B150, 2023.
- 951 Tiberia, A., Mascitelli, A., D’adderio, L.P., Federico, S., Marisaldi, M., Porcù, F., Realini, E.,
952 Gatti, A., Ursi, A., Fuschino, F. and Tavani, M.: Time evolution of storms producing terrestrial
953 gamma-ray flashes using ERA5 reanalysis data, GPS, lightning and geostationary satellite
954 observations. *Remote Sensing*, *13*(4), 784, 2021.
- 955 Vaquero-Martínez, J. and Antón, M.: Review on the role of GNSS meteorology in monitoring
956 water vapor for atmospheric physics, *Remote Sensing*, *13*(12), 2287,
957 <https://doi.org/10.3390/rs13122287>, 2021.
- 958 Viticchie, B., Lekouara, M., Hungershofer, K., Joro, S., Grandell, J., Maufrais, A., Marquez, M.J.,
959 Munro, R.: Algorithm Theoretical Basis Document (ATBD) for L2 processing of the MTG
960 Lightning Imager data, Rapp. Tech. EUMESTAT, 6, 2020.
- 961 Waxler, R., Frazier, W. G., Talmadge, C. L., Liang, B., Hetzer, C., Buchanan, H., and Audette, W.
962 E.: Analysis of infrasound array data from tornadic storms in the southeastern United States,
963 *Journal of the Acoustical Society of America*, *156*, 1903–1919,
964 <https://doi.org/10.1121/10.0028815>, 2024.

- 965 Wessel, P., Luis, J.F., Uieda, L.A., Scharroo, R., Wobbe, F., Smith, W.H. and Tian, D.: The generic
966 mapping tools version 6, *Geochemistry, Geophysics, Geosystems*, 20(11), 5556-5564,
967 <https://doi.org/10.1029/2019GC008515>, 2019.
- 968 Wilgan, K., Rohm, W. and Bosy, J.: Multi-observation meteorological and GNSS data comparison
969 with numerical weather prediction model, *Atmospheric Research*, 156, 29–42,
970 <https://doi.org/10.1016/j.atmosres.2014.12.011>, 2015.
- 971 Wu, G., Qin, S., Mao, Y., Ma, Z. and Shi, C.: Validation of precipitation events in ERA5 to gauge
972 observations during warm seasons over eastern China. *Journal of Hydrometeorology*, 23(5), 807-
973 822, 2022.
- 974